# An isogeometric Reissner-Mindlin shell element based on Bézier dual basis functions: overcoming locking and improved coarse mesh accuracy

Z. Zou[1], M.A. Scott[1], D. Miao[1], M. Bischoff[2], B. Oesterle[2], and W. Dornisch[3]

[1]Department of Civil and Environmental Engineering, Brigham Young University, Provo, UT USA
[2]Institute for Structural Mechanics, University of Stuttgart, Stuttgart, Germany
[3]Fachgebiet Statik und Dynamik, Brandenburgische Technische Universität Cottbus-Senftenberg, Cottbus, Germany

2020-06-02

## Abstract

We develop a mixed geometrically nonlinear isogeometric Reissner-Mindlin shell element for the analysis of thin-walled structures that leverages Bézier dual basis functions to address both shear and membrane locking and to improve the quality of computed stresses. The accuracy of computed solutions over coarse meshes, that have highly non-interpolatory control meshes, is achieved through the application of a continuous rotational approach. The starting point of the formulation is the modified Hellinger-Reissner variational principle with independent displacement, membrane, and shear strains as the unknown fields. To overcome locking, the strain variables are interpolated with lower-order spline bases while the variations of the strain variables are interpolated with the corresponding Bézier dual bases. Leveraging the orthogonality property of the Bézier dual basis, the strain variables are condensed out of the system with only a slight increase in the bandwidth of the resulting linear system. The condensed approach preserves the accuracy of the non-condensed mixed approach but with fewer degrees of freedom. From a practical point of view, since the Bézier dual basis is completely specified through Bézier extraction, any spline space that admits Bézier extraction can utilize the proposed approach directly.

*Keywords:* shells; isogeometric analysis; Reissner-Mindlin; locking; dual basis; Bézier extraction

## 1 Introduction

Thin-walled shell structures are widely used in engineering due to their high ratio of load capacity to weight. To model these types of structures with finite element analysis (FEA) shell elements are often used. Commercial FEA is dominated by shell elements derived from the shear-deformable Reissner-Mindlin (RM) shell theories since they can be discretized with standard $C^0$ basis functions. Additionally, the rotational degrees of freedom of a RM formulation can be leveraged to easily accommodate rotational boundary conditions, geometry with kinks, and non-manifold connections. Recently, isogeometric methods based on $C^1$-smooth (or higher) splines and the Kirchhoff-Love (KL) thin shell theory have increased in popularity. These methods are computationally efficient since they do not require rotational degrees of freedom. However, the absence of rotational degrees of freedom makes modeling complex structural assemblies with KL shells difficult.

A major challenge in using higher-order smooth splines to discretize shell theories is numerical locking. The primary sources of locking are shear and membrane locking. In shear locking, pure inextensional bending modes are polluted by parasitic shear strains and, in membrane locking, pure inextensional bending modes are polluted by parasitic membrane strains. While not a major contributor to locking for low-order (linear) shell elements, membrane locking is particularly vexing for higher-order curved shell elements. In this sense,

shell elements based on smooth splines are more prone to locking than their low-order counterparts. All locking effects can be ameliorated by increasing the degree of the basis functions, but for quadratic and cubic basis functions, the workhorse degrees in isogeometric shell analysis, locking can still destroy the accuracy of computed shell solutions, especially in thin shell regimes. In particular, computed stresses can be completely spurious.

## 1.1  Key contributions

The specific contributions of this paper are:

- A mixed nonlinear isogeometric RM shell formulation is developed which is capable of alleviating both shear and membrane locking and improving the quality of shear and membrane stresses. Similar to what was done in [11], the strains are split into appropriate shear and membrane strain components which are then interpolated directly with lower-order bases.

- An efficient technique utilizing the Bézier dual spline basis [58, 44] is used to condense out the strain variables in the mixed shell formulation. This technique preserves the sparsity of the resulting stiffness matrix and preserves the accuracy of displacement and stress solutions produced by the non-condensed mixed formulation.

- The proposed dual basis is specified completely in terms of the Bézier extraction of a given spline space making it simple to extend the approach to any piecewise polynomial spline space (e.g., T-splines, hierarchical splines, LR-splines, U-splines, etc.).

- Both continuous and discrete rotational approaches [20, 19, 21] are used in the mixed setting to update the director orientation. It is demonstrated for the first time, that, when locking is eliminated for $p = 2, 3$, the inaccuracy of the *discrete* rotation approach prevents accurate solution behavior for coarse mesh layouts, thus eliminating one of the most powerful arguments for using IGA shells for practical problems where reducing element count is paramount. This is particularly true in the large displacement and rotation setting. The *continuous* rotation approach, on the other hand, produces highly accurate results for coarse mesh layouts.

- An efficient scheme for updating the current director and its derivatives is proposed. It is equivalent to the scheme proposed in [19, 21] but avoids updating the rotation tensor and its derivatives at each Newton-Raphson iteration and reduces the storage cost by two thirds at each quadrature point or node for the continuous and discrete rotational approaches, respectively.

## 1.2  Prior work

Various techniques have been proposed to address locking in finite element shells. Prominent among these approaches are mixed formulations based on generalized variational principles [39, 54, 37] with displacement, strain and/or stress unknowns, the reduced and selective integration techniques [57, 31, 33], the assumed strain method [34, 29, 46, 4, 13, 38], and the enhanced assumed strain method [16, 12]. To some extent, the last three methods are equivalent to a mixed formulation under specific conditions [43, 50, 2].

The reduced and selective integration techniques are dominant in commercial low-order (linear) finite elements due to their simplicity, efficiency, and robustness. However, the reduced integration method may introduce spurious zero energy modes, which is a serious defect requiring some form of stabilization [7]. The selective reduced integration technique is less efficient than the reduced integration approach in terms of the computational efficiency and is usually restricted to cases where the material properties of the shell do not vary through the thickness. The assumed strain method interpolates selected strain components with specially constructed lower-order basis functions, while the enhanced assumed strain method attaches additional terms to the selected strains and introduces extra strain variables that can then be condensed out on the element level. Although these two methods can remove shear and/or membrane locking for $C^0$ continuous shell elements, they are not as effective if higher-order continuous basis is used.

Isogeometric Analysis (IGA), introduced by Hughes et al. [32], adopts the Computer Aided Design (CAD) description as the basis for analysis. CAD technologies like Non-Uniform Rational B-splines (NURBS) [47],

subdivision surfaces [55], and T-splines [49, 48] make it possible to define smooth higher-order basis functions over both structured and unstructured meshes. This has opened the door to new shell formulations based on both RM and KL shell kinematics [10, 8, 9, 35, 21, 28].

Since the CAD geometry is represented in the analysis, quantities such as curvature, tangents, and normals are immediately accessible and exact. However, despite the advantages of IGA in shell analysis, locking behavior persists [22] and, in fact, higher-order smoothness introduces additional challenges such as pronounced membrane locking [1]. Several traditional finite element techniques for mitigating locking have been extended to IGA shells [17, 1, 21, 25, 14, 36]. Those approaches most closely related to the proposed approach include Bouclier et al. [14] where a mixed isogeometric solid-shell element was developed that leverages local quasi-interpolation for the strain variables which are then condensed out locally without calculating the inverse of a large Gramian matrix. Despite some accuracy loss when compared to the non-condensed mixed formulation, this method leads to a sparse stiffness matrix, therefore improving the computational efficiency. By approximating the strain variables through a local $L^2$-projection [52], Greco et al [26] proposed a similar formulation to remove membrane locking in curved Kirchhoff rods and showed that a smooth strain interpolation is necessary to achieve accurate results. This approach is then applied to isogeometric KL shells in [25].

By leveraging $C^1$-smoothness, several new shear-deformable shell formulations have been proposed which are based on a hierarchical decomposition of the director in the deformed configuration [45, 40, 23, 6]. These approaches eliminate shear locking *a priori* while permitting shear deformations. Recently, Bieber et al. [11] proposed the mixed displacement method. This approach defines mixed strain components to be some derivatives of auxiliary displacement variables. In this way, both shear and membrane locking can be alleviated in a pure displacement-based formulation (i.e., no lower-order spaces have to be explicitly constructed). However, this method introduces extra non-physical auxiliary variables and the application of the gradient operator to these variables introduces additional zero energy modes into the system which must be removed with appropriate boundary conditions. It also requires the second derivatives of basis functions to release membrane locking.

The outline of this paper is as follows. In Section 2 fundamental spline concepts are reviewed including a description of the Bézier dual basis. Section 3 describes nonlinear Reissner-Mindlin shell kinematics. Two different definitions of the rotation of the director commonly used in shear deformable shells, i.e., the continuous and discrete rotations of the director vector, are introduced in Section 4. Section 5 introduces the mixed variational formulations which are the starting point for our formulations. We then describe the interpolation scheme for the assumed shear and membrane strains in Section 6 and propose an efficient technique, based on Bézier dual basis functions, to condense out the assumed strain variables in Section 7. Several challenging benchmark problems are then solved in Section 8 followed by conclusions in Section 9.

# 2　Spline fundamentals

## 2.1　Spline bases

The $I$th Bernstein polynomial of degree $p$ on $[\xi_1, \xi_2]$ can be defined as

$$B_I^p(\xi) = \binom{p}{I-1} \left( \frac{\xi_2 - \xi}{\xi_2 - \xi_1} \right)^{p-I+1} \left( \frac{\xi - \xi_1}{\xi_2 - \xi_1} \right)^{I-1}, \tag{1}$$

where $\binom{p}{I-1} = \frac{p!}{(I-1)!(p-I+1)!}$ is a binomial coefficient. A univariate quadratic Bernstein basis on $[0, 1]$ is shown in Figure 1a. A degree $p$ Bézier curve in $\mathbb{R}^d$ can be written as

$$\mathbf{x}(\xi) = \sum_{I=1}^{p+1} \mathbf{P}_I B_I^p(\xi), \quad \xi \in [\xi_1, \xi_2] \tag{2}$$

where $\mathbf{P}_I \in \mathbb{R}^d$ is called a control point.
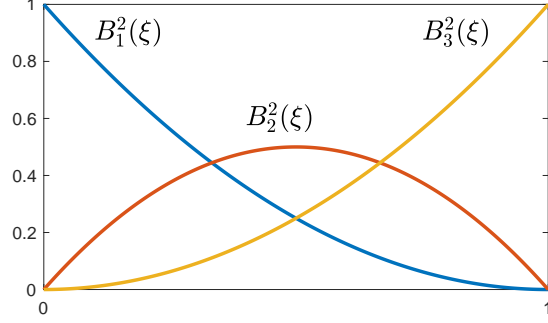
(a) Bernstein basis on $[0, 1]$.
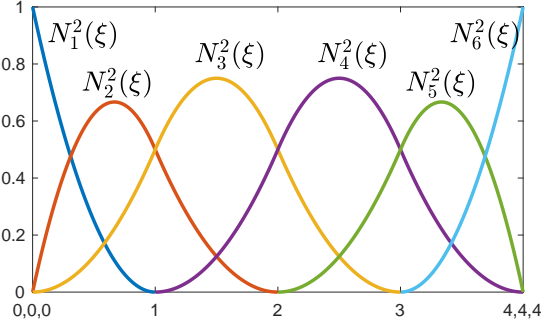


(b) B-spline basis, $\Xi = \{0, 0, 0, 1, 2, 3, 4, 4, 4\}$.
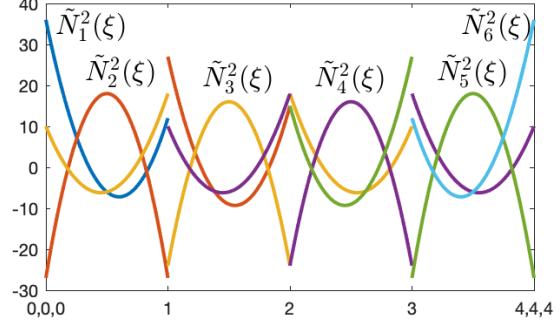


(c) The Bézier dual basis corresponding to the B-spline basis in Figure 1b.

Figure 1: A univariate quadratic Bernstein basis (a), a univariate quadratic $C^1$ B-spline basis (b), and the Bézier dual basis (c) corresponding to the B-spline basis in (b).

A univariate B-spline basis is defined by a knot vector $\Xi = \{\xi_1, \xi_2, \ldots, \xi_{n+p+1}\}$, which consists of a non-decreasing sequence of real numbers, $\xi_I \leq \xi_{I+1}, I = 1, \ldots, n+p+1$, where $p$ is the degree of the B-spline basis and $n$ is the number of basis functions. The $I$th B-spline basis function of degree $p$, denoted by $N_I^p(\xi)$, can be recursively defined

$$N_I^0(\xi) = \begin{cases} 1, & \text{if} \quad \xi_I \leq \xi < \xi_{I+1} \\ 0, & \text{otherwise} \end{cases}$$

$$N_I^p(\xi) = \frac{\xi - \xi_I}{\xi_{I+p} - \xi_I} N_I^{p-1}(\xi) + \frac{\xi_{I+p+1} - \xi}{\xi_{I+p+1} - \xi_{I+1}} N_{I+1}^{p-1}(\xi).$$

A univariate quadratic B-spline basis is illustrated in Figure 1b.

A B-spline curve of degree $p$ can be written as

$$\mathbf{x}(\xi) = \sum_{I=1}^{n} \mathbf{P}_I N_I^p(\xi), \quad \xi \in [\xi_1, \xi_{n+p+1}]. \tag{3}$$

A $p$th-degree NURBS curve can be represented as

$$\mathbf{x}(\xi) = \sum_{I=1}^{n} \mathbf{P}_I w_I R_I^p(\xi), \quad \xi \in [\xi_1, \xi_{n+p+1}] \tag{4}$$

where the NURBS basis function $R_I^p$ is defined by

$$R_I^p(\xi) = \frac{N_I^p(\xi)}{W(\xi)} \tag{5}$$

where $N_I^p(\xi)$ is the $I$th $p$-degree B-spline basis function,

$$W(\xi) = \sum_{I=1}^{n} w_I N_I^p(\xi) \tag{6}$$

is a weighting function, and $w_I$ is the weight corresponding to control point $\mathbf{P}_I$. Since a NURBS curve is a rational polynomial, it can be used to exactly represent conic sections. Higher dimensional analogs to these concepts can be created using tensor products or more advanced construction schemes like hierarchical B-splines [24] and T-splines [49].

## 2.2  Bézier dual bases

In this section, we introduce the Bézier dual basis by simply following the procedures and similar notation conventions given in [58]. For conciseness, we only give properties that are used in subsequent sections. Interested readers are referred to [58] for more details.

The Bézier dual basis, defined over the physical domain of an element $e$, denoted by $\Omega^e$, can be written as

$$\tilde{\mathbf{N}}^e = \mathrm{diag}(\boldsymbol{\omega}^e)(\mathbf{R}^e)^T (\mathbf{G}_{B,B}^e)^{-1} \mathbf{B}^e = \mathbf{D}^e \mathbf{B}^e \tag{7}$$

where $\mathbf{B}^e$ is the set of Bernstein polynomials defined on element $e$,

$$\mathbf{G}_{B,B}^e = \left[ \int_{\Omega^e} B_i^e(\xi) B_j^e(\xi)\, \mathrm{d}\Omega \right] \tag{8}$$

is the Gramian matrix for the Bernstein basis, $\mathbf{R}^e$ is the element reconstruction operator [52], $\mathbf{D}^e$ is the dual element extraction operator [58] and $\boldsymbol{\omega}^e$ is a vector of smooth weights whose $i$th component is defined as

$$\omega_i^e = \frac{\int_{\hat{\Omega}^e} N_I\, \mathrm{d}\hat{\Omega}}{\int_{\hat{\Omega}^I} N_I\, \mathrm{d}\hat{\Omega}} \tag{9}$$

where $\hat{\Omega}^e$ is the parametric domain of an element and $\hat{\Omega}^I$ is the parametric support of basis function $N_I$.

In this way, we can easily verify that the inner product of the dual basis $\tilde{\mathbf{N}}^e$ and the B-spline basis $\mathbf{N}^e$ on element $e$ satisfies

$$\int_{\Omega^e} \tilde{\mathbf{N}}^e (\mathbf{N}^e)^{\mathrm{T}} \mathrm{d}\Omega = \mathrm{diag}(\boldsymbol{\omega}^e). \tag{10}$$

After the standard finite element assembly, we get the biorthogonality condition over the physical domain $\Omega$ on patch level as

$$\int_{\Omega} \tilde{\mathbf{N}} \mathbf{N}^{\mathrm{T}} \mathrm{d}\Omega = \mathbf{I}. \tag{11}$$

If rational basis functions are used, we define the dual basis as

$$\tilde{R}_I = W \frac{\tilde{N}_I}{w_I} \tag{12}$$

where $W$ is a rational weighting function and $w_I$ is the control point weight. A univariate Bézier dual basis corresponding to the B-spline basis shown in Figure 1b is shown in Figure 1c.

# 3  Shell kinematics
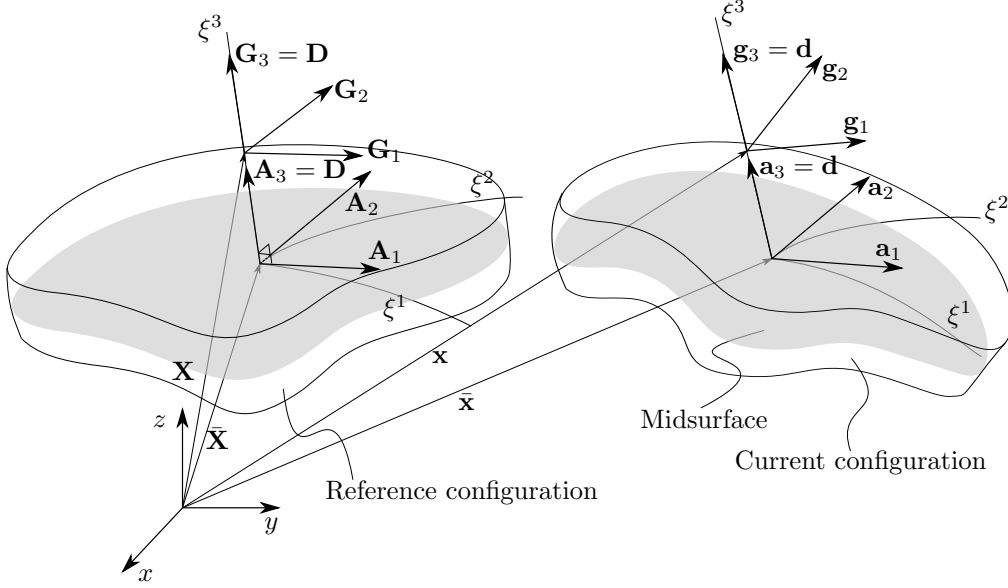


Figure 2: A schematic of shell kinematics.

The reference and current configurations of a shell-like body, as illustrated in Figure 2, are parameterized as

$$\mathbf{X}(\xi^1,\xi^2,\xi^3) = \bar{\mathbf{X}}(\xi^1,\xi^2) + \xi^3 \mathbf{D}(\xi^1,\xi^2), \tag{13}$$

$$\mathbf{x}(\xi^1,\xi^2,\xi^3) = \bar{\mathbf{x}}(\xi^1,\xi^2) + \xi^3 \mathbf{d}(\xi^1,\xi^2) \tag{14}$$

where $-\frac{h}{2} \le \xi^3 \le \frac{h}{2}$, $\bar{\mathbf{X}}$ and $\bar{\mathbf{x}}$ denote the midsurfaces, and $\mathbf{D}$ and $\mathbf{d}$ denote the directors in the reference and current configurations, respectively. Note that we will adopt the established convention for Latin and Greek indices (i.e., $i = 1, 2, 3$ and $\alpha = 1, 2$).

The base vectors of the midsurfaces can be written as

$$\mathbf{A}_\alpha = \bar{\mathbf{X}}_{,\alpha}, \quad \mathbf{A}_3 = \mathbf{D} = \frac{\mathbf{A}_1 \times \mathbf{A}_2}{|\mathbf{A}_1 \times \mathbf{A}_2|}, \tag{15}$$

$$\mathbf{a}_\alpha = \bar{\mathbf{x}}_{,\alpha}, \quad \mathbf{a}_3 = \mathbf{d} \tag{16}$$

where $(\cdot)_{,\alpha}$ denotes $\partial(\cdot)/\partial\xi^\alpha$. The covariant base vectors at any point in the shell continuum are defined as

$$\mathbf{G}_\alpha = \mathbf{X}_{,\alpha} = \bar{\mathbf{X}}_{,\alpha} + \xi^3 \mathbf{D}_{,\alpha} = \mathbf{A}_\alpha + \xi^3 \mathbf{D}_{,\alpha} \quad \mathbf{G}_3 = \mathbf{X}_{,3} = \mathbf{D}, \tag{17}$$

$$\mathbf{g}_\alpha = \mathbf{x}_{,\alpha} = \bar{\mathbf{x}}_{,\alpha} + \xi^3 \mathbf{d}_{,\alpha} = \mathbf{a}_\alpha + \xi^3 \mathbf{d}_{,\alpha} \quad \mathbf{g}_3 = \mathbf{x}_{,3} = \mathbf{d}. \tag{18}$$

The Green-Lagrange strain tensor $\mathbf{E}$ is defined as

$$\mathbf{E} = \frac{1}{2}(\mathbf{F}^{\mathrm{T}}\mathbf{F} - \mathbf{I}) \tag{19}$$

where $\mathbf{F} = \mathrm{d}\mathbf{x}/\mathrm{d}\mathbf{X}$ is called the material deformation gradient and $\mathbf{I}$ is the identity tensor. In components, the Green-Lagrange strain can be written as

$$E_{ij} = \frac{1}{2}(g_{ij} - G_{ij}) \tag{20}$$

where

$$g_{ij} = \mathbf{g}_i \cdot \mathbf{g}_j, \quad G_{ij} = \mathbf{G}_i \cdot \mathbf{G}_j. \tag{21}$$

Substituting (17) and (18) into (20) and neglecting the higher order terms of $\xi^3$, we can get the components of the Green-Lagrange strain as

$$E_{\alpha\beta} = \frac{1}{2}\left[(\mathbf{a}_\alpha \cdot \mathbf{a}_\beta + \xi^3 \mathbf{a}_\alpha \cdot \mathbf{d}_{,\beta} + \xi^3 \mathbf{d}_{,\alpha} \cdot \mathbf{a}_\beta) - (\mathbf{A}_\alpha \cdot \mathbf{A}_\beta + \xi^3 \mathbf{A}_\alpha \cdot \mathbf{D}_{,\beta} + \xi^3 \mathbf{D}_{,\alpha} \cdot \mathbf{A}_\beta)\right], \tag{22}$$

$$E_{\alpha 3} = \frac{1}{2}\left(\mathbf{a}_\alpha \cdot \mathbf{d} + \xi^3 \mathbf{d}_{,\alpha} \cdot \mathbf{d} - \mathbf{A}_\alpha \cdot \mathbf{D} - \xi^3 \mathbf{D}_{,\alpha} \cdot \mathbf{D}\right), \tag{23}$$

$$E_{33} = \frac{1}{2}\left(\mathbf{d} \cdot \mathbf{d} - \mathbf{D} \cdot \mathbf{D}\right). \tag{24}$$

The inextensibility assumption of the director, i.e. $||\mathbf{d}|| = 1$, leads to

$$\mathbf{d} \cdot \mathbf{d} = \mathbf{D} \cdot \mathbf{D} = 1, \tag{25}$$

$$\mathbf{d}_{,\alpha} \cdot \mathbf{d} = \mathbf{D}_{,\alpha} \cdot \mathbf{D} = 0 \tag{26}$$

and according to the definition of $\mathbf{D}$ we also have that $\mathbf{A}_\alpha \cdot \mathbf{D} = 0$ and $\mathbf{A}_\alpha \cdot \mathbf{D}_{,\beta} = -\mathbf{D} \cdot \mathbf{A}_{\alpha,\beta} = \mathbf{D}_{,\alpha} \cdot \mathbf{A}_\beta$. As a consequence, (22) to (24) become

$$E_{\alpha\beta} = \frac{1}{2}\left[(\mathbf{a}_\alpha \cdot \mathbf{a}_\beta - \mathbf{A}_\alpha \cdot \mathbf{A}_\beta) + \xi^3(\mathbf{a}_\alpha \cdot \mathbf{d}_{,\beta} + \mathbf{d}_{,\alpha} \cdot \mathbf{a}_\beta - 2\mathbf{D}_{,\beta} \cdot \mathbf{A}_\alpha\right], \tag{27}$$

$$E_{\alpha 3} = \frac{1}{2}\mathbf{a}_\alpha \cdot \mathbf{d}, \tag{28}$$

$$E_{33} = 0. \tag{29}$$

Rewriting the non-zero strains with Voigt notation results in

$$\mathbf{E} = \begin{bmatrix} \boldsymbol{\epsilon} + \xi^3 \boldsymbol{\kappa} \\ \boldsymbol{\gamma} \end{bmatrix} \tag{30}$$

where $\boldsymbol{\epsilon}$, $\boldsymbol{\kappa}$ and $\boldsymbol{\gamma}$ are the membrane, bending, and shear strains, respectively, which are defined as

$$\boldsymbol{\epsilon} = \begin{bmatrix} \epsilon_{11} \\ \epsilon_{22} \\ 2\epsilon_{12} \end{bmatrix}, \quad \boldsymbol{\kappa} = \begin{bmatrix} \kappa_{11} \\ \kappa_{22} \\ 2\kappa_{12} \end{bmatrix}, \quad \text{and} \quad \boldsymbol{\gamma} = \begin{bmatrix} \gamma_1 \\ \gamma_2 \end{bmatrix} \tag{31}$$

where

$$\epsilon_{\alpha\beta} = \frac{1}{2}(\mathbf{a}_\alpha \cdot \mathbf{a}_\beta - \mathbf{A}_\alpha \cdot \mathbf{A}_\beta), \tag{32}$$

$$\kappa_{\alpha\beta} = \frac{1}{2}(\mathbf{a}_\alpha \cdot \mathbf{d}_{,\beta} + \mathbf{d}_{,\alpha} \cdot \mathbf{a}_\beta) - \mathbf{D}_{,\beta} \cdot \mathbf{A}_\alpha, \tag{33}$$

$$\gamma_\alpha = \mathbf{a}_\alpha \cdot \mathbf{d}. \tag{34}$$

The first variation of the strain components can be written as

$$\delta\epsilon_{\alpha\beta} = \frac{1}{2}(\delta\bar{\mathbf{x}}_{,\alpha} \cdot \bar{\mathbf{x}}_{,\beta} + \delta\bar{\mathbf{x}}_{,\beta} \cdot \bar{\mathbf{x}}_{,\alpha}),$$

$$\delta\kappa_{\alpha\beta} = \frac{1}{2}(\delta\bar{\mathbf{x}}_{,\alpha} \cdot \mathbf{d}_{,\beta} + \delta\bar{\mathbf{x}}_{,\beta} \cdot \mathbf{d}_{,\alpha} + \delta\mathbf{d}_{,\alpha} \cdot \bar{\mathbf{x}}_{,\beta} + \delta\mathbf{d}_{,\beta} \cdot \bar{\mathbf{x}}_{,\alpha}), \tag{35}$$

$$\delta\gamma_\alpha = \delta\bar{\mathbf{x}}_{,\alpha} \cdot \mathbf{d} + \delta\mathbf{d} \cdot \bar{\mathbf{x}}_{,\alpha}$$

and the second variation as

$$\Delta\delta\epsilon_{\alpha\beta} = \frac{1}{2}(\delta\bar{\mathbf{x}}_{,\alpha} \cdot \Delta\bar{\mathbf{x}}_{,\beta} + \delta\bar{\mathbf{x}}_{,\beta} \cdot \Delta\bar{\mathbf{x}}_{,\alpha}), \tag{36}$$

$$\Delta\delta\kappa_{\alpha\beta} = \frac{1}{2}(\delta\bar{\mathbf{x}}_{,\alpha} \cdot \Delta\mathbf{d}_{,\beta} + \delta\bar{\mathbf{x}}_{,\beta} \cdot \Delta\mathbf{d}_{,\alpha} + \delta\mathbf{d}_{,\alpha} \cdot \Delta\bar{\mathbf{x}}_{,\beta} + \delta\mathbf{d}_{,\beta} \cdot \Delta\bar{\mathbf{x}}_{,\alpha} \tag{37}$$

$$+ \bar{\mathbf{x}}_{,\alpha} \cdot \Delta\delta\mathbf{d}_{,\beta} + \bar{\mathbf{x}}_{,\beta} \cdot \Delta\delta\mathbf{d}_{,\alpha}), \tag{38}$$

$$\Delta\delta\gamma_\alpha = \delta\bar{\mathbf{x}}_{,\alpha} \cdot \Delta\mathbf{d} + \delta\mathbf{d} \cdot \Delta\bar{\mathbf{x}}_{,\alpha} + \bar{\mathbf{x}}_{,\alpha} \cdot \Delta\delta\mathbf{d}. \tag{39}$$

# 4 Director definition

In this section, we describe both a continuous and discrete approaches to define shell directors in the current configuration. In [19, 27, 21], the continuous approach calculates the current director by rotating the *initial* director at each quadrature point, while the discrete approach calculates the current director by interpolating current nodal directors which are also obtained by rotating the *initial* nodal directors. In both cases, a rotation tensor and its derivative need to be updated and stored at each quadrature point or node, respectively.

The present work follows the same update framework, however, the current directors at quadrature points in the continuous approach or at nodes in the discrete approach are obtained by rotating the *previous* directors at the corresponding locations. In this way, we only need to calculate and store the current director and its derivative information at each quadrature point or node rather than a rotation tensor and its derivatives, which reduces computational cost and storage. It can be easily shown that the proposed method is equivalent to that in [27, 20, 19, 21]. The derivations of the variations of the directors and their derivatives follow standard approaches [19, 27, 21]. For additional details see Appendices B and C.

## 4.1 The continuous approach

In this case, the current director is defined as

$$\mathbf{d}^i(\xi^\alpha) = \Delta \mathbf{R} \mathbf{d}^{i-1}(\xi^\alpha) \tag{40}$$

where the superscripts $i$ and $i-1$ indicate the Newton-Raphson iterate, $\Delta \mathbf{R}$ is the incremental rotation tensor, and

$$\Delta \mathbf{R} = \mathbf{I} + c_1 \Delta \mathbf{\Omega} + c_2 \Delta \mathbf{\Omega}^2 \quad c_1 = \frac{\sin \Delta\omega}{\Delta\omega} \quad c_2 = \frac{1 - \cos \Delta\omega}{\Delta\omega^2} \quad \Delta\omega = |\Delta\boldsymbol{\omega}| \tag{41}$$

where $\Delta\boldsymbol{\omega} = \Delta\boldsymbol{\omega}(\xi^\alpha) \in \mathbb{R}^d$ is the axial vector of the global incremental rotation at each quadrature point and

$$\Delta \mathbf{\Omega} = \text{skew} \, \Delta\boldsymbol{\omega} = \begin{bmatrix} 0 & -\Delta\omega_3 & \Delta\omega_2 \\ \Delta\omega_3 & 0 & -\Delta\omega_1 \\ -\Delta\omega_2 & \Delta\omega_1 & 0 \end{bmatrix}. \tag{42}$$

The derivatives of the director can be written as

$$\mathbf{d}^i_{,\alpha} = \Delta \mathbf{R}_{,\alpha} \mathbf{d}^{i-1} + \Delta \mathbf{R} \mathbf{d}^{i-1}_{,\alpha}, \tag{43}$$

where

$$\Delta \mathbf{R}_{,\alpha} = c_{1,\alpha} \Delta \mathbf{\Omega} + c_1 \Delta \mathbf{\Omega}_{,\alpha} + c_{2,\alpha} \Delta \mathbf{\Omega}^2 + c_2 (\Delta \mathbf{\Omega}_{,\alpha} \Delta \mathbf{\Omega} + \Delta \mathbf{\Omega} \Delta \mathbf{\Omega}_{,\alpha}) \tag{44}$$

$$\Delta \mathbf{\Omega}_{,\alpha} = \text{skew} \, \Delta\boldsymbol{\omega}_{,\alpha} \quad c_{1,\alpha} = \Delta\omega_{,\alpha} \frac{\Delta\omega \cos \Delta\omega - \sin \Delta\omega}{\Delta\omega^2} \quad c_{2,\alpha} = \Delta\omega_{,\alpha} \frac{\Delta\omega \sin \Delta\omega - 2 + 2\cos \Delta\omega}{\Delta\omega^3} \tag{45}$$

$$\Delta\omega_{,\alpha} = \frac{\Delta\boldsymbol{\omega}_{,\alpha} \cdot \Delta\boldsymbol{\omega}}{\Delta\omega}. \tag{46}$$

Note that when $\Delta\omega$ is very small we choose

$$c_1 = 1 \,, \quad c_2 = \frac{1}{2} \quad \text{and} \quad c_{1,\alpha} = c_{2,\alpha} = \Delta\omega_{,\alpha} = 0 \tag{47}$$

to ensure numerical stability.

It is shown in Appendix A that the above approach to calculate $\mathbf{d}^i$ and $\mathbf{d}^i_{,\alpha}$ is equivalent to the approach in [19, 27, 21] except that only $\mathbf{d}^{i-1}$ and $\mathbf{d}^{i-1}_{,\alpha}$ need to be stored rather than $\mathbf{R}^{i-1}$ and $\mathbf{R}^{i-1}_{,\alpha}$, therefore reducing the number of variables stored at each quadrature point from 27 to 9.

8

## 4.2 The discrete approach

In this case, the current director is defined through the interpolation of the current nodal directors $\mathbf{d}_I$ as

$$\mathbf{d}^h = \sum_I N_I \mathbf{d}_I \quad \text{and} \quad \mathbf{d}^h_{,\alpha} = \sum_I N_{I,\alpha} \mathbf{d}_I \tag{48}$$

where

$$\mathbf{d}_I = \Delta\mathbf{R}(\Delta\boldsymbol{\omega}_I)\mathbf{d}_I^{i-1} \tag{49}$$

$$\Delta\boldsymbol{\omega}_I = \mathbf{T}_{3I}\Delta\beta_I. \tag{50}$$

Note that $\Delta\mathbf{R}(\Delta\boldsymbol{\omega}_I)$ is calculated by inserting the nodal increment of the axial vector $\Delta\boldsymbol{\omega}_I$ into (41) and $\mathbf{T}_{3I}$ is defined in (99). Again, we only store nodal director information at nodes.

# 5 Variational formulation

## 5.1 The Hu-Washizu variational theorem

The Hu-Washizu functional can be written as

$$\Pi_{HW}(\mathbf{u}, \bar{\mathbf{E}}, \bar{\mathbf{S}}) = \frac{1}{2}\int_\Omega \bar{\mathbf{E}}^\mathrm{T}\bar{\mathbf{S}}\,\mathrm{d}\Omega - \int_\Omega \bar{\mathbf{S}}^\mathrm{T}(\bar{\mathbf{E}} - \mathbf{E})\,\mathrm{d}\Omega - \int_{\Gamma_u}(\bar{\mathbf{S}}\mathbf{n})^\mathrm{T}(\mathbf{u} - \mathbf{u}_0)\,\mathrm{d}\Gamma + \Pi_{ext}(\mathbf{u}) \tag{51}$$

where

$$\Pi_{ext}(\mathbf{u}) = -\int_\Omega \mathbf{u}^\mathrm{T}\mathbf{F}_b\,d\Omega - \int_{\Gamma_t}\mathbf{u}^\mathrm{T}\mathbf{F}_t\,d\Gamma_t \tag{52}$$

and $\mathbf{u}$, $\bar{\mathbf{E}}$, and $\bar{\mathbf{S}}$ are the unknown displacement, strain, and stress *variables*, $\mathbf{E}$ is the Green-Lagrange strain defined in (30), $\mathbf{F}_b$ and $\mathbf{F}_t$ are the body force and traction, which act on the continuum body $\Omega$ and the traction boundary $\Gamma_\sigma$, respectively. For simplicity, we assume that the loads $\mathbf{F}_b$ and $\mathbf{F}_t$ are independent of the body deformation.

The Hu-Washizu variational theorem can be simply written as

$$\Pi_{HW}(\mathbf{u}, \bar{\mathbf{E}}, \bar{\mathbf{S}}) = Stationary. \tag{53}$$

## 5.2 The Hellinger-Reissner variational theorem

For Saint-Venant Kirchhoff materials, if we let the displacement boundary condition and the stress-strain relation be satisfied strongly, i.e.,

$$\mathbf{u} = \mathbf{u}_0 \quad \text{on } \Gamma_u \tag{54}$$

$$\bar{\mathbf{S}} = \mathbf{C}\bar{\mathbf{E}} \quad \text{on } \Omega \tag{55}$$

where $\mathbf{C}$ is the elasticity matrix and $\mathbf{u}_0$ is the prescribed displacement on boundary $\Gamma_u$ then the Hu-Washizu functional can be written as

$$\Pi_{HR}(\mathbf{u}, \bar{\mathbf{E}}) = \int_\Omega \left(\mathbf{E}^\mathrm{T}\mathbf{C}\bar{\mathbf{E}} - \frac{1}{2}\bar{\mathbf{E}}^\mathrm{T}\mathbf{C}\bar{\mathbf{E}} - \mathbf{u}^\mathrm{T}\mathbf{F}_b\right)\mathrm{d}\Omega - \int_{\Gamma_t}\mathbf{u}^\mathrm{T}\mathbf{F}_t\mathrm{d}\Gamma_t. \tag{56}$$

This is often called a modified Hellinger-Reissner functional as the strains, instead of stresses, are taken as the extra unknowns. At this point, (56) no longer depends on unknown stresses $\bar{\mathbf{S}}$ since they have been eliminated through the strong satisfaction of the constitutive law in (55).

The Hellinger-Reissner variational theorem can be written as

$$\Pi_{HR}(\mathbf{u}, \bar{\mathbf{E}}) = Stationary. \tag{57}$$

Invoking the stationarity of $\Pi_{HR}(\mathbf{u}, \bar{\mathbf{E}})$ results in

$$\delta\Pi_{HR}(\mathbf{u}, \delta\mathbf{u}, \bar{\mathbf{E}}, \delta\bar{\mathbf{E}}) = \int_\Omega \delta\mathbf{E}^\mathrm{T}\mathbf{C}\bar{\mathbf{E}} - \delta\bar{\mathbf{E}}^\mathrm{T}\mathbf{C}(\bar{\mathbf{E}} - \mathbf{E})\mathrm{d}\Omega$$

$$-\int_\Omega \delta\mathbf{u}^\mathrm{T}\mathbf{F}_b\mathrm{d}\Omega - \int_{\Gamma_t} \delta\mathbf{u}^\mathrm{T}\mathbf{F}_t\mathrm{d}\Gamma_t = 0. \tag{58}$$

The linearization of the above stationary conditions yields

$$L[\delta\Pi_{HR}(\mathbf{u}, \delta\mathbf{u}, \bar{\mathbf{E}}, \delta\bar{\mathbf{E}})] := \delta\Pi_{HR}(\mathbf{u}, \delta\mathbf{u}, \bar{\mathbf{E}}, \delta\bar{\mathbf{E}}) + \Delta\delta\Pi_{HR}(\Delta\mathbf{u}, \delta\mathbf{u}, \Delta\bar{\mathbf{E}}, \delta\bar{\mathbf{E}}) = 0 \tag{59}$$

where

$$\Delta\delta\Pi_{HR}(\Delta\mathbf{u}, \delta\mathbf{u}, \Delta\bar{\mathbf{E}}, \delta\bar{\mathbf{E}}) = \int_\Omega \underbrace{-\delta\bar{\mathbf{E}}^\mathrm{T}\mathbf{C}\Delta\bar{\mathbf{E}} + \delta\bar{\mathbf{E}}^\mathrm{T}\mathbf{C}\Delta\mathbf{E} + \delta\mathbf{E}^\mathrm{T}\mathbf{C}\Delta\bar{\mathbf{E}}}_{\text{material stiffness}}$$

$$+ \underbrace{\Delta\delta\mathbf{E}^\mathrm{T}\mathbf{C}\bar{\mathbf{E}} - \Delta\delta\bar{\mathbf{E}}^\mathrm{T}\mathbf{C}(\bar{\mathbf{E}} - \mathbf{E})}_{\text{geometric stiffness}}\Big)\mathrm{d}\Omega. \tag{60}$$

Note that we defined the Green-Lagrange strain in terms of covariant components in Section 3. Therefore, the elasticity matrix $\mathbf{C}$ should be represented in contravariant components, which can be obtained from the components defined in the Cartesian coordinate system through a matrix transformation, see [56] for details.

# 6  Discretization of the mixed variational form

## 6.1  Strain variable discretization

To eliminate membrane and shear locking, the assumed strains are defined as

$$\bar{\mathbf{E}} = \begin{bmatrix} \bar{\boldsymbol{\epsilon}} + \xi^3\boldsymbol{\kappa} \\ \bar{\boldsymbol{\gamma}} \end{bmatrix} \tag{61}$$

where the bending strains, $\boldsymbol{\kappa}$, are not modified. If membrane locking is negligible, the membrane strain components, $\boldsymbol{\epsilon}$, can also remain unchanged, i.e., $\bar{\boldsymbol{\epsilon}} = \boldsymbol{\epsilon}$. The assumed membrane and shear strains are interpolated with carefully chosen lower-order bases as

$$\bar{\boldsymbol{\epsilon}} = \begin{bmatrix} \bar{\epsilon}_1 \\ \bar{\epsilon}_2 \\ \bar{\epsilon}_3 \end{bmatrix} = \begin{bmatrix} \sum_{A=1}^{n_a} N_A^{p-1,q}\bar{\epsilon}_{A1} \\ \sum_{B=1}^{n_b} N_B^{p,q-1}\bar{\epsilon}_{B2} \\ \sum_{C=1}^{n_c} N_C^{p-1,q-1}\bar{\epsilon}_{C3} \end{bmatrix}, \quad \bar{\boldsymbol{\gamma}} = \begin{bmatrix} \bar{\gamma}_1 \\ \bar{\gamma}_2 \end{bmatrix} = \begin{bmatrix} \sum_{A=1}^{n_a} N_A^{p-1,q}\bar{\gamma}_{A1} \\ \sum_{B=1}^{n_b} N_B^{p,q-1}\bar{\gamma}_{B2} \end{bmatrix}, \tag{62}$$

where $n_a$, $n_b$ and $n_c$ are the basis function numbers of the selectively reduced lower-order bases $\{N_A^{p-1,q}\}_{A=1}^{n_a}$, $\{N_B^{p,q-1}\}_{B=1}^{n_b}$, and $\{N_C^{p-1,q-1}\}_{C=1}^{n_c}$ with $p$ and $q$ the degrees of the primal basis in $\xi$ and $\eta$ directions, respectively. The first variation of the assumed strains can be written as

$$\delta\bar{\boldsymbol{\epsilon}} = \begin{bmatrix} \sum_{A=1}^{n_a} N_A^{p-1,q}\delta\bar{\epsilon}_{A1} \\ \sum_{B=1}^{n_b} N_B^{p,q-1}\delta\bar{\epsilon}_{B2} \\ \sum_{C=1}^{n_c} N_C^{p-1,q-1}\delta\bar{\epsilon}_{C3} \end{bmatrix}, \quad \delta\bar{\boldsymbol{\gamma}} = \begin{bmatrix} \sum_{A=1}^{n_a} N_A^{p-1,q}\delta\bar{\gamma}_{A1} \\ \sum_{B=1}^{n_b} N_B^{p,q-1}\delta\bar{\gamma}_{B2} \end{bmatrix}, \tag{63}$$

and the second variations vanish. In this formulation, the assumed strain variables (62) and its variations (63) are discretized using the same function spaces, which leads to the so-called Bubnov-Galerkin formulation.

This choice of interpolation of the strain variables is inspired by the mixed displacement method [11], where some derivatives of the original primal basis are used to interpolate different strain components as

follows,

$$\bar{\boldsymbol{\epsilon}} = \begin{bmatrix} \bar{\epsilon}_1 \\ \bar{\epsilon}_2 \\ \bar{\epsilon}_3 \end{bmatrix} = \begin{bmatrix} \bar{u}_{1,1} \\ \bar{u}_{2,2} \\ \bar{u}_{3,12} \end{bmatrix} = \sum_{A=1}^{n_p} \begin{bmatrix} N_{A,1}^{p,q} \bar{u}_{A1} \\ N_{A,2}^{p,q} \bar{u}_{A2} \\ N_{A,12}^{p,q} \bar{u}_{A3} \end{bmatrix}, \quad \bar{\boldsymbol{\gamma}} = \begin{bmatrix} \bar{\gamma}_1 \\ \bar{\gamma}_2 \end{bmatrix} = \begin{bmatrix} \bar{v}_{1,1} \\ \bar{v}_{2,2} \end{bmatrix} = \sum_{A=1}^{n_p} \begin{bmatrix} N_{A,1}^{p,q} \bar{v}_{A1} \\ N_{B,2}^{p,q} \bar{v}_{A2} \end{bmatrix} \tag{64}$$

where $\bar{u}_i$ and $\bar{v}_\alpha$ are called the mixed displacements, and $n_p$ is the number of primal basis functions. It can be easily verified that the spans of the lower-order bases used in (62) are the same as the derivative spaces utilized in (64) with appropriate constraints given in [11]. These lower-order bases have also been used in [23] and [25] to release membrane locking for geometrically linear problems. The effectiveness of these interpolation schemes for releasing both shear and membrane locking is demonstrated numerically in Section 8 for geometrically linear and nonlinear problems. A theoretical exploration of the *inf-sup* stability of the resulting discretizations [3, 15] in the regime of higher-order continuous isogeometric shell elements will not be explored in this paper.

## 6.2 Matrix formulation

Substituting (30) and (61) into the linearized stationary condition (59) gives

$$\int_\Omega - \begin{bmatrix} \delta\bar{\boldsymbol{\epsilon}} + \xi^3 \delta\boldsymbol{\kappa} \\ \delta\bar{\boldsymbol{\gamma}} \end{bmatrix}^{\mathrm{T}} \mathbf{C} \begin{bmatrix} \Delta\bar{\boldsymbol{\epsilon}} + \xi^3 \Delta\boldsymbol{\kappa} \\ \Delta\bar{\boldsymbol{\gamma}} \end{bmatrix} + \begin{bmatrix} \delta\bar{\boldsymbol{\epsilon}} + \xi^3 \delta\boldsymbol{\kappa} \\ \delta\bar{\boldsymbol{\gamma}} \end{bmatrix}^{\mathrm{T}} \mathbf{C} \begin{bmatrix} \Delta\boldsymbol{\epsilon} + \xi^3 \Delta\boldsymbol{\kappa} \\ \Delta\boldsymbol{\gamma} \end{bmatrix} + \begin{bmatrix} \delta\boldsymbol{\epsilon} + \xi^3 \delta\boldsymbol{\kappa} \\ \delta\boldsymbol{\gamma} \end{bmatrix}^{\mathrm{T}} \mathbf{C} \begin{bmatrix} \Delta\bar{\boldsymbol{\epsilon}} + \xi^3 \Delta\boldsymbol{\kappa} \\ \Delta\bar{\boldsymbol{\gamma}} \end{bmatrix}$$
$$+ \begin{bmatrix} \Delta\delta\boldsymbol{\epsilon} + \xi^3 \Delta\delta\boldsymbol{\kappa} \\ \Delta\delta\boldsymbol{\gamma} \end{bmatrix}^{\mathrm{T}} \mathbf{C} \begin{bmatrix} \bar{\boldsymbol{\epsilon}} + \xi^3 \boldsymbol{\kappa} \\ \bar{\boldsymbol{\gamma}} \end{bmatrix} - \begin{bmatrix} \xi^3 \Delta\delta\boldsymbol{\kappa} \\ \mathbf{0} \end{bmatrix}^{\mathrm{T}} \mathbf{C} \left( \begin{bmatrix} \bar{\boldsymbol{\epsilon}} + \xi^3 \boldsymbol{\kappa} \\ \bar{\boldsymbol{\gamma}} \end{bmatrix} - \begin{bmatrix} \boldsymbol{\epsilon} + \xi^3 \boldsymbol{\kappa} \\ \boldsymbol{\gamma} \end{bmatrix} \right) \mathrm{d}\Omega =$$
$$- \int_\Omega \begin{bmatrix} \delta\boldsymbol{\epsilon} + \xi^3 \delta\boldsymbol{\kappa} \\ \delta\boldsymbol{\gamma} \end{bmatrix}^{\mathrm{T}} \mathbf{C} \begin{bmatrix} \bar{\boldsymbol{\epsilon}} + \xi^3 \boldsymbol{\kappa} \\ \bar{\boldsymbol{\gamma}} \end{bmatrix} + \begin{bmatrix} \delta\bar{\boldsymbol{\epsilon}} + \xi^3 \delta\boldsymbol{\kappa} \\ \delta\bar{\boldsymbol{\gamma}} \end{bmatrix}^{\mathrm{T}} \mathbf{C} \left( \begin{bmatrix} \bar{\boldsymbol{\epsilon}} + \xi^3 \boldsymbol{\kappa} \\ \bar{\boldsymbol{\gamma}} \end{bmatrix} - \begin{bmatrix} \boldsymbol{\epsilon} + \xi^3 \boldsymbol{\kappa} \\ \boldsymbol{\gamma} \end{bmatrix} \right) \mathrm{d}\Omega$$
$$+ \int_\Omega \delta\mathbf{u}^{\mathrm{T}} \mathbf{F}_b \mathrm{d}\Omega + \int_{\Gamma_t} \delta\mathbf{u}^{\mathrm{T}} \mathbf{F}_t \mathrm{d}\Gamma_t \mathrm{d}\Gamma_e. \tag{65}$$

We define the primal displacement/rotation and assumed strain nodal vectors by

$$\hat{\mathbf{U}} = \begin{bmatrix} \mathbf{u}_1 \\ \boldsymbol{\beta}_1 \\ \vdots \\ \mathbf{u}_I \\ \boldsymbol{\beta}_I \\ \vdots \\ \mathbf{u}_{n_p} \\ \boldsymbol{\beta}_{n_p} \end{bmatrix} \quad \text{and} \quad \hat{\mathbf{E}} = \begin{bmatrix} \hat{\mathbf{E}}^m \\ \hat{\mathbf{E}}^s \end{bmatrix}, \tag{66}$$

respectively, where $\mathbf{u}_I$ and $\boldsymbol{\beta}_I$ are the displacement and rotation unknowns corresponding to the $I$th primal node, $\hat{\mathbf{E}}^m$ and $\hat{\mathbf{E}}^s$ are the assumed membrane and shear strain nodal vectors associated with the three different lower-order bases in (62), which are defined as

$$\hat{\mathbf{E}}^m = \begin{bmatrix} \bar{\epsilon}_{11} & \dots & \bar{\epsilon}_{I1} & \dots & \bar{\epsilon}_{n_a 1} & \bar{\epsilon}_{12} & \dots & \bar{\epsilon}_{I2} & \dots & \bar{\epsilon}_{n_b 2} & \bar{\epsilon}_{13} & \dots & \bar{\epsilon}_{I3} & \dots & \bar{\epsilon}_{n_c 3} \end{bmatrix}^{\mathrm{T}}$$

and

$$\hat{\mathbf{E}}^s = \begin{bmatrix} \bar{\gamma}_{11} & \dots & \bar{\gamma}_{I1} & \dots & \bar{\gamma}_{n_a 1} & \bar{\gamma}_{12} & \dots & \bar{\gamma}_{I2} & \dots & \bar{\gamma}_{n_b 2} \end{bmatrix}^{\mathrm{T}},$$

where $\bar{\epsilon}_{Ii}, \bar{\gamma}_{Ii}$ are membrane and shear strain unknowns of the $I$th assumed strain node of the $i$th lower-order basis.

Inserting the interpolations of the variations of displacement, assumed strains, and Green-Lagrange strain components (119), (120), and (121) into the linearized stationary condition (65) leads to the linear system solved at each Newton-Raphson iteration

$$
\begin{bmatrix} \mathbf{K}_{11}^{mat} + \mathbf{K}^{geom} & \mathbf{K}_{12}^{mat} \\ \mathbf{K}_{21}^{mat} & \mathbf{K}_{22}^{mat} \end{bmatrix} \begin{bmatrix} \Delta\hat{\mathbf{U}} \\ \Delta\hat{\mathbf{E}} \end{bmatrix} = \begin{bmatrix} \hat{\mathbf{F}}_{ext} - \hat{\mathbf{F}}_{int}^b \\ -\hat{\mathbf{F}}_{int}^{ms} \end{bmatrix},
\tag{67}
$$

where the material stiffness matrices $\mathbf{K}_{\alpha\beta}^{mat}$ are defined as

$$
\mathbf{K}_{11}^{mat} = \int_\Omega (\mathbf{B}^b)^{\mathrm{T}} \mathbf{C} \mathbf{B}^{ms} + (\mathbf{B}^b + \mathbf{B}^{ms})^{\mathrm{T}} \mathbf{C} \mathbf{B}^b \, \mathrm{d}\Omega,
\tag{68}
$$

$$
\mathbf{K}_{12}^{mat} = \int_\Omega (\mathbf{B}^{ms})^{\mathrm{T}} \mathbf{C} \bar{\mathbf{B}}^{ms} \, \mathrm{d}\Omega,
\tag{69}
$$

$$
\mathbf{K}_{21}^{mat} = \int_\Omega (\bar{\mathbf{B}}^{ms})^{\mathrm{T}} \mathbf{C} \mathbf{B}^{ms} \, \mathrm{d}\Omega,
\tag{70}
$$

$$
\mathbf{K}_{22}^{mat} = \int_\Omega -(\bar{\mathbf{B}}^{ms})^{\mathrm{T}} \mathbf{C} \bar{\mathbf{B}}^{ms} \, \mathrm{d}\Omega.
\tag{71}
$$

Here the superscripts $b$ and $ms$ indicate that the strain-displacement matrices $\mathbf{B}^b$ and $\mathbf{B}^{ms}$ are derived from the variations of *bending* and *membrane* and *shear* strains, respectively. These strain-displacement matrices can be written as

$$
\mathbf{B}_I^b = \xi^3 \begin{bmatrix} N_{I,1}\mathbf{d}_{,1}^{h\mathrm{T}} & \bar{\mathbf{x}}_{,1}^{h\mathrm{T}}\mathbf{T}_{I,1} \\ N_{I,2}\mathbf{d}_{,2}^{h\mathrm{T}} & \bar{\mathbf{x}}_{,2}^{h\mathrm{T}}\mathbf{T}_{I,2} \\ N_{I,2}\mathbf{d}_{,1}^{h\mathrm{T}} + N_{I,1}\mathbf{d}_{,2}^{h\mathrm{T}} & \bar{\mathbf{x}}_{,1}^{h\mathrm{T}}\mathbf{T}_{I,2} + \bar{\mathbf{x}}_{,2}^{h\mathrm{T}}\mathbf{T}_{I,1} \\ \mathbf{0} & \mathbf{0} \end{bmatrix}
\tag{72}
$$

and

$$
\mathbf{B}_I^{ms} = \begin{bmatrix} N_{I,1}\bar{\mathbf{x}}_{,1}^{h\mathrm{T}} & \mathbf{0} \\ N_{I,2}\bar{\mathbf{x}}_{,2}^{h\mathrm{T}} & \mathbf{0} \\ N_{I,1}\bar{\mathbf{x}}_{,2}^{h\mathrm{T}} + N_{I,2}\bar{\mathbf{x}}_{,1}^{h\mathrm{T}} & \mathbf{0} \\ N_{I,1}\mathbf{d}^{h\mathrm{T}} & \bar{\mathbf{x}}_{,1}^{hT}\mathbf{T}_I \\ N_{I,2}\mathbf{d}^{h\mathrm{T}} & \bar{\mathbf{x}}_{,2}^{hT}\mathbf{T}_I \end{bmatrix}.
\tag{73}
$$

The strain-displacement matrix $\bar{\mathbf{B}}^{ms}$ is derived from the variations of assumed *membrane* and *shear* strains (63). As there are three types of assumed strain nodes, it is written at the element level as

$$
\bar{\mathbf{B}}_e^{ms} = \begin{bmatrix} N_1^{p-1,q} & 0 & 0 & 0 & 0 \\ \vdots & \vdots & \vdots & \vdots & \vdots \\ N_l^{p-1,q} & 0 & 0 & 0 & 0 \\ 0 & N_1^{p,q-1} & 0 & 0 & 0 \\ \vdots & \vdots & \vdots & \vdots & \vdots \\ 0 & N_m^{p,q-1} & 0 & 0 & 0 \\ 0 & 0 & N_1^{p-1,q-1} & 0 & 0 \\ \vdots & \vdots & \vdots & \vdots & \vdots \\ 0 & 0 & N_n^{p-1,q-1} & 0 & 0 \\ 0 & 0 & 0 & N_1^{p-1,q} & 0 \\ \vdots & \vdots & \vdots & \vdots & \vdots \\ 0 & 0 & 0 & N_l^{p-1,q} & 0 \\ 0 & 0 & 0 & 0 & N_1^{p,q-1} \\ \vdots & \vdots & \vdots & \vdots & \vdots \\ 0 & 0 & 0 & 0 & N_m^{p,q-1} \end{bmatrix}^{\mathrm{T}}
\tag{74}
$$

where $l$, $m$, and $n$ denote the numbers of the three different strain node types defined over the $e$th element.

The $IK^{th}$ nodal submatrix of the geometric stiffness matrix $\mathbf{K}^{geom}$ can be written as

$$\mathbf{K}_{IK}^{geom} = \int_{\Omega} \begin{bmatrix} \mathbf{K}_{IK_{11}}^{geom} & \mathbf{K}_{IK_{12}}^{geom} \\ \mathbf{K}_{IK_{21}}^{geom} & \mathbf{K}_{IK_{22}}^{geom} \end{bmatrix} \mathrm{d}\Omega$$

where

$$\mathbf{K}_{IK_{11}}^{geom} = (N_{I,1}N_{K,1}\bar{S}^{11} + N_{I,2}N_{K,2}\bar{S}^{22} + N_{I,1}N_{K,2}\bar{S}^{12} + N_{I,2}N_{K,1}\bar{S}^{21})\mathbf{I},$$

$$\mathbf{K}_{IK_{12}}^{geom} = \xi^3 S^{11}N_{I,1}\mathbf{T}_{K,1} + \xi^3 S^{22}N_{I,2}\mathbf{T}_{K,2} + \xi^3 S^{12}(N_{I,1}\mathbf{T}_{K,2} + N_{I,2}\mathbf{T}_{K,1}) + (\bar{S}^{13}N_{I,1} + \bar{S}^{23}N_{I,2})\mathbf{T}_K,$$

$$\mathbf{K}_{IK_{21}}^{geom} = \xi^3 S^{11}N_{K,1}\mathbf{T}_{I,1}^{\mathrm{T}} + \xi^3 S^{22}N_{K,2}\mathbf{T}_{I,2}^{\mathrm{T}} + \xi^3 S^{12}(N_{K,1}\mathbf{T}_{I,2}^{\mathrm{T}} + N_{K,2}\mathbf{T}_{I,1}^{\mathrm{T}}) + (\bar{S}^{13}N_{K,1} + \bar{S}^{23}N_{K,2})\mathbf{T}_I^{\mathrm{T}},$$

$$\mathbf{K}_{IK_{22}}^{geom} = \xi^3 S^{11}\hat{\mathbf{m}}_{IK,1}^{\beta\beta}(\bar{\mathbf{x}}_{,1}^h) + \xi^3 S^{22}\hat{\mathbf{m}}_{IK,2}^{\beta\beta}(\bar{\mathbf{x}}_{,2}^h) + \xi^3 S^{12}(\hat{\mathbf{m}}_{IK,1}^{\beta\beta}(\bar{\mathbf{x}}_{,2}^h) + \hat{\mathbf{m}}_{IK,2}^{\beta\beta}(\bar{\mathbf{x}}_{,1}^h)) + \bar{S}^{13}\hat{\boldsymbol{q}}_{IK}^{\beta\beta}(\bar{\mathbf{x}}_{,1}^h) + \bar{S}^{23}\hat{\boldsymbol{q}}_{IK}^{\beta\beta}(\bar{\mathbf{x}}_{,2}^h).$$

Here $S^{ij}$ are the components of second Piola-Kirchhoff stress $\mathbf{S}$, and $\bar{S}^{ij}$ are the stress components calculated from the assumed strains, i.e.,

$$\bar{\mathbf{S}} = \mathbf{C}\bar{\mathbf{E}}. \tag{75}$$

The internal force vectors $\hat{\mathbf{F}}_{int}^b$ and $\hat{\mathbf{F}}_{int}^{ms}$ are defined as

$$\hat{\mathbf{F}}_{int}^b = \int_{\Omega} (\mathbf{B}^{ms})^{\mathrm{T}}\bar{\mathbf{S}} + \xi^3(\mathbf{B}^b)^{\mathrm{T}}\mathbf{S} \, \mathrm{d}\Omega \tag{76}$$

$$\hat{\mathbf{F}}_{int}^{ms} = \int_{\Omega} (\bar{\mathbf{B}}^{ms})^{\mathrm{T}}(\mathbf{S} - \bar{\mathbf{S}}) \, \mathrm{d}\Omega. \tag{77}$$

The external force vector $\hat{\mathbf{F}}_{ext}$ is calculated using standard approaches for RM shells [30]. We use numerical integration through the thickness of the shell. Analytical preintegration can be used if the shifter tensor is assumed to be the identity [21].

# 7 Condensation of assumed strain variables

The mixed shell formulation described previously effectively alleviates locking as will be shown numerically in Section 8. However, it can introduce up to five additional degrees of freedom per assumed strain node. In traditional $C^0$ RM shell elements, the assumed strain fields are discontinuous along element interfaces and can be easily condensed out at the element level. However, for higher-order smooth shell elements this is no longer possible and alternative approaches must be employed. We devise an approach based on Bézier dual basis functions that preserves the sparsity of the resulting stiffness matrix and accuracy of the original mixed formulation.

## 7.1 Strain variable discretization and matrix formulation

We now define the variations of the assumed strains $\delta\bar{\boldsymbol{\epsilon}}$ and $\delta\bar{\boldsymbol{\gamma}}$ as

$$\delta\bar{\boldsymbol{\epsilon}} = \frac{1}{h}\mathbf{C}^{-\mathrm{T}} \begin{bmatrix} \sum_{A=1}^{n_a} \tilde{N}_A^{p-1,q}\delta\bar{\epsilon}_{A1} \\ \sum_{B=1}^{n_b} \tilde{N}_B^{p,q-1}\delta\bar{\epsilon}_{B2} \\ \sum_{C=1}^{n_c} \tilde{N}_C^{p-1,q-1}\delta\bar{\epsilon}_{C3} \end{bmatrix}, \quad \text{and} \quad \delta\bar{\boldsymbol{\gamma}} = \frac{1}{h}\mathbf{C}^{-\mathrm{T}} \begin{bmatrix} \sum_{A=1}^{n_a} \tilde{N}_A^{p-1,q}\delta\bar{\gamma}_{A1} \\ \sum_{B=1}^{n_b} \tilde{N}_B^{p,q-1}\delta\bar{\gamma}_{B2} \end{bmatrix}, \tag{78}$$

where $\tilde{N}_A^{p-1,q}$, $\tilde{N}_B^{p,q-1}$ and $\tilde{N}_C^{p-1,q-1}$ are the Bézier dual bases corresponding to $N_A^{p-1,q}$, $N_B^{p,q-1}$ and $N_C^{p-1,q-1}$ defined in Section 2.2 and $h$ is the shell thickness. Since the assumed strain variables (62) and its variations (78) are discretized using different function spaces this is a so-called Petrov-Galerkin formulation.

In this case, the structure of the resulting linear systems remains the same as (67) where now $\mathbf{K}_{21}^{mat}$ and $\mathbf{K}_{22}^{mat}$ are defined as

$$\mathbf{K}_{21}^{mat} = \int_{\Omega} (\tilde{\mathbf{B}}^{ms})^{\mathrm{T}} \mathbf{B}^{ms} \, \mathrm{d}\Omega \tag{79}$$

$$\mathbf{K}_{22}^{mat} = \int_{\Omega} -(\tilde{\mathbf{B}}^{ms})^{\mathrm{T}} \bar{\mathbf{B}}^{ms} \, \mathrm{d}\Omega \tag{80}$$

where $\mathbf{B}^{ms}$ and $\bar{\mathbf{B}}^{ms}$ are the same as those defined in Section 6.2, and $\tilde{\mathbf{B}}^{ms}$ is defined at element level as

$$\tilde{\mathbf{B}}_e^{ms} = \frac{1}{h} \begin{bmatrix} \tilde{N}_1^{p-1,q} & 0 & 0 & 0 & 0 \\ \vdots & \vdots & \vdots & \vdots & \vdots \\ \tilde{N}_l^{p-1,q} & 0 & 0 & 0 & 0 \\ 0 & \tilde{N}_1^{p,q-1} & 0 & 0 & 0 \\ \vdots & \vdots & \vdots & \vdots & \vdots \\ 0 & \tilde{N}_m^{p,q-1} & 0 & 0 & 0 \\ 0 & 0 & \tilde{N}_1^{p-1,q-1} & 0 & 0 \\ \vdots & \vdots & \vdots & \vdots & \vdots \\ 0 & 0 & \tilde{N}_n^{p-1,q-1} & 0 & 0 \\ 0 & 0 & 0 & \tilde{N}_1^{p-1,q} & 0 \\ \vdots & \vdots & \vdots & \vdots & \vdots \\ 0 & 0 & 0 & \tilde{N}_l^{p-1,q} & 0 \\ 0 & 0 & 0 & 0 & \tilde{N}_1^{p,q-1} \\ \vdots & \vdots & \vdots & \vdots & \vdots \\ 0 & 0 & 0 & 0 & \tilde{N}_m^{p,q-1} \end{bmatrix}^{\mathrm{T}} . \tag{81}$$

When calculating $\mathbf{K}_{22}^{mat}$ we assume that the basis vectors $\mathbf{G}_i$ are constant through the thickness. This assumption and the biorthogonality condition of the dual basis (11) means that

$$\mathbf{K}_{22}^{mat} = \int_{\Omega} -(\tilde{\mathbf{B}}^{ms})^{\mathrm{T}} \bar{\mathbf{B}}^{ms} \, \mathrm{d}\Omega = -\mathbf{I}. \tag{82}$$

Therefore, the assumed strain variables can be easily condensed out leading to the linear system

$$\left( \mathbf{K}_{11}^{mat} + \mathbf{K}_{12}^{mat} \mathbf{K}_{21}^{mat} + \mathbf{K}^{geom} \right) \Delta \hat{\mathbf{U}} = \hat{\mathbf{F}}_{ext} - \hat{\mathbf{F}}_{int}^b - \mathbf{K}_{12}^{mat} \hat{\mathbf{F}}_{int}^{ms}. \tag{83}$$

Notice that no inverse matrix is required and the final stiffness matrix

$$\mathbf{K} = \mathbf{K}_{11}^{mat} + \mathbf{K}_{12}^{mat} \mathbf{K}_{21}^{mat} + \mathbf{K}^{geom} \tag{84}$$

remains sparse with a slighly wider bandwidth. Figure 3 shows the sparsity patterns for the stiffness matrices computed for the Scordelis-Lo roof problem in Section 8.3. Note that as the assumed strains and their variations are discretized with different basis functions, we have $(\mathbf{K}_{12}^{mat})^{\mathrm{T}} \neq \mathbf{K}_{21}^{mat}$. As a consequence, the resulting stiffness matrix (84) is nonsymmetric which can slightly increase the computational cost in solving the system of equations compared to a case with a symmetric stiffness matrix having the same size and sparsity pattern.

The geometric stiffness matrix $\mathbf{K}^{geom}$, the external force vector $\hat{\mathbf{F}}_{ext}$, and the internal force vector $\hat{\mathbf{F}}_{int}^b$ remain unchanged and are computed as described in Section 6.2. However, the internal force vector $\hat{\mathbf{F}}_{int}^{ms}$ is now defined as

$$\hat{\mathbf{F}}_{int}^{ms} = \int_{\Omega} (\tilde{\mathbf{B}}^{ms})^{\mathrm{T}} \mathbf{C}^{-1} (\mathbf{S} - \bar{\mathbf{S}}) \, \mathrm{d}\Omega. \tag{85}$$

Within each Newton-Raphson iteration the assumed strain unknowns $\Delta \hat{\mathbf{E}}^{ms}$ can be recovered as

$$\Delta \hat{\mathbf{E}}^{ms} = \mathbf{K}_{21}^{mat} \Delta \hat{\mathbf{U}} + \hat{\mathbf{F}}_{int}^{ms}. \tag{86}$$
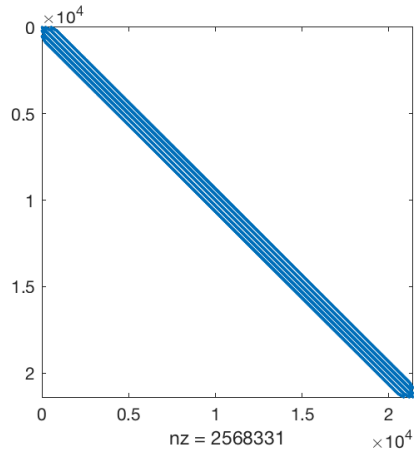
(a) Displacement-based formulation.
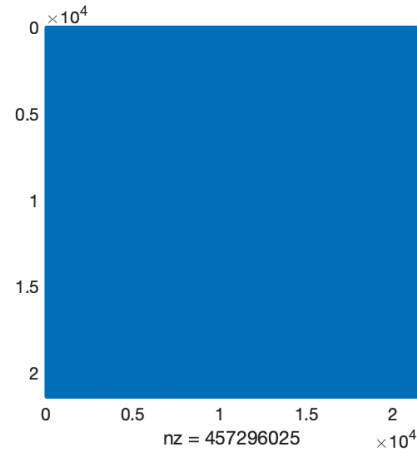
(b) Mixed Bubnov-Galerkin formulation.
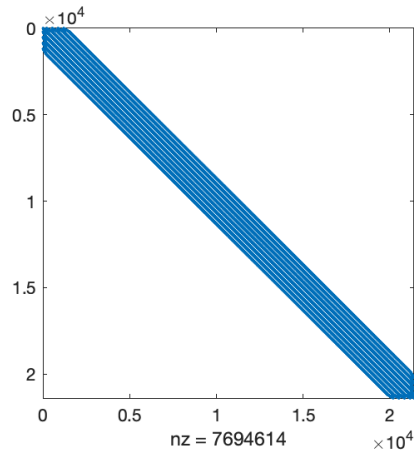
(c) Mixed Petrov-Galerkin formulation.

Figure 3: Stiffness matrix sparsity patterns for the Scordelis-Lo roof problem in Section 8.3, 64 elements per side. (a) a standard displacement-based RM formulation, (b) the mixed Bubnov-Galerkin formulation with strain variables condensed out, (c) the proposed Petrov-Galerkin formulation with strain variables condensed out.

# 8 Numerical examples

We now evaluate the performance of the proposed mixed shell formulations on several benchmark problems. Several different shell elements are compared:

- KL: *Kirchhoff-Love* shell [35].

- RMC: *Reissner-Mindlin* shell with *continuous* rotations of the director [27, 19, 21].

- RMD: *Reissner-Mindlin* shell with *discrete* rotations of the director [20, 19, 21].

- RMCMD: *Reissner-Mindlin* shell with *continuous* rotations of the director, based on the *mixed* displacement method [11].

- RMCM: *Reissner-Mindlin* shell with *continuous* rotations of the director, based on the *mixed* Bubnov-Galerkin formulation.

- RMDM: *Reissner-Mindlin* shell with *discrete* rotations of the director, based on the *mixed* Bubnov-Galerkin formulation.

- RMCMP: *Reissner-Mindlin* shell with *continuous* rotations of the director, based on the *mixed Petrov-Galerkin* formulation.

## 8.1 Cylindrical shell subject to transverse loading in the radial direction

Figure 4 shows the schematic for a cylindrical shell subject to transverse loading in the radial direction. This model has a radius $R = 10$, a width $b = 1$, and a varying thickness. Young's modulus and Poisson's ratio are $E = 1000$ and $\nu = 0$, respectively. The cylindrical shell is clamped at one end and subject to a traction, $q_x = 0.1t^3$, at the other end. An analytical solution based on Bernoulli beam theory gives an approximate value of 0.942 for the radial displacement at the free end. This problem is modeled with quadratic and cubic NURBS of maximal smoothness. The initial mesh has $2 \times 1$ elements, and uniform refinement is applied in the circumferential direction.

Figure 5 shows the convergence of the maximum tip displacement $u_x$ with varying slendernesses $\frac{R}{t} = 100, 1000$, and 10000. As can be seen, for $p = 2, 3$ and all slendernesses, the standard isogeometric shells RMC and RMD lock severely for the coarse meshes when compared with the proposed RMCM shell, which nearly obtains the reference solution with the initial mesh. The locking increases as the slenderness increases. For $p = 2$, RMC and RMD shells are comparable. For $p = 3$, and $\frac{R}{t} = 100$ the RMD shell achieves better results than the RMC shell as shown in Figure 5a. This can be attributed to the fact that the error from the discrete rotation of the director softens the system response [21]. However, this improvement disappears as the slenderness increases as shown in Figure 5b and c.

Figure 6 compares the convergence behaviors of the maximum tip displacement $u_x$ for RMCM, RMDM and RMCMP shells. As can be seen, The RMDM shell is less accurate than the RMCM shell. This is because, once locking has been alleviated, the inaccuracy inherent in the discrete rotation of the director manifests itself. This inaccuracy worsens with increasing degree [21]. The proposed RMCMP shell obtains comparable results as the RMCM shell but with strain variables condensed out. It can be also seen that for a fixed degree, these three types shells do not lock as the slenderness increases. This is not the case for the standard RMC and RMD shells as shown in Figure 5, which lock severely as the slenderness increases. This demonstrates that these mixed formulations eliminate membrane and shear locking effectively.

The proposed mixed shell formulations also accurately capture stresses. This is in stark contrast to standard isogeometric shells. Figure 7 shows the computed membrane force $n_{\phi\phi}$ for quadratic RMC, RMCM and RMCMP shell elements. The analytical solution of the membrane force is 0 at the free end and $-0.1t^3$ at the fixed end. As can be seen, with 10 elements the membrane force for the RMC shell oscillates significantly, especially for increasing slenderness, and the maximum and minimum forces are several orders of magnitude off from the analytical solution. In contrast, the proposed RMCM and RMCMP shells achieve almost the same smooth and accurate results.
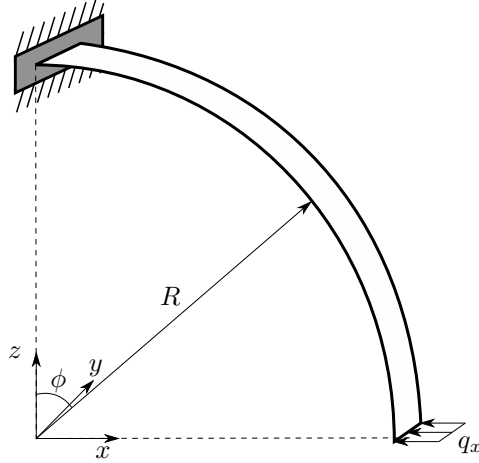
Figure 4: A cylindrical shell subject to transverse loading in the radial direction.

## 8.2 Clamped square plate subject to a uniformly distributed load

We now analyze a clamped square plate subject to a uniform distributed load as shown in Figure 8a. The square plate has length $L = 10$, Young's modulus $E = 1000$, and Poisson's ratio $\nu = 0.3$. The thickness $t$ is varied to give a slenderness ratio $\frac{L}{t} = 100$, 1000 and 10000. The distributed load is set to $q = t^3$. The maximum displacement at the center of the plate is monitored. The exact solution is $u_{max} = -0.138$ for all thicknesses [53]. Due to symmetry, only one quarter of the geometry is modeled.

To demonstrate the behavior of our approach for a distorted mesh configuration, the initial mesh consists of only one quadratic element with skewed control net as shown in Figure 8b. Figure 9 shows the behavior of the RMC, RMCM and RMCMP shells for increasing slenderness. It can be seen that the standard RMC shell locks significantly in all cases, especially for lower-order basis functions and thin geometry. The RMCM and RMCMP shell show superior behavior for all orders $p = 2, 3$ and slendernesses $\frac{L}{t} = 100, 1000, 10000$ in terms of accuracy per degree of freedom. Note that as the shell gets thinner, the mixed shell formulations start to converge slower with coarse meshes, which is mainly due to the more severe boundary layer phenomenon [18].

The contour plots of transverse shear stress $\sigma_{xz}$ at the midsurface with $\frac{L}{t} = 100$ and $16 \times 16$ maximally smooth quadratic elements are shown in Figure 10b, c and d. A numerical reference using $64 \times 64$ maximally smooth $p = 5$ RMC shell elements is shown in Figure 10a. As can be seen, significant oscillations occur for the standard RMC shell with $16 \times 16$ quadratic elements. The superiority of the RMCM and RMCMP elements in representing the shear stress is clear and the RMCMP shell obtains even better stress than the RMCM shell. Note that to show the symmetric distribution of the stress the whole geometry is modeled here and the initial mesh adopts the same skewed control net configuration as shown in Figure 8b but with full geometry size.
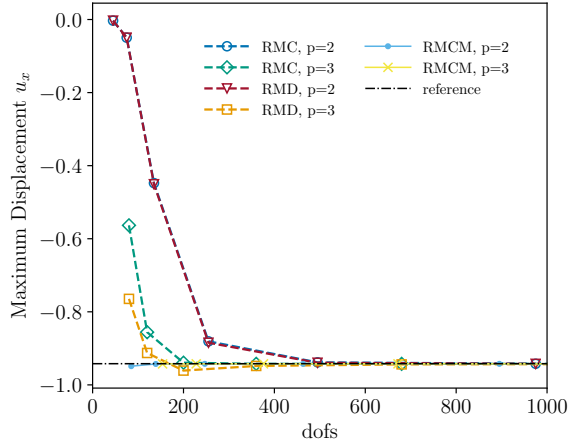
(a) Slenderness $\frac{R}{t} = 100$.
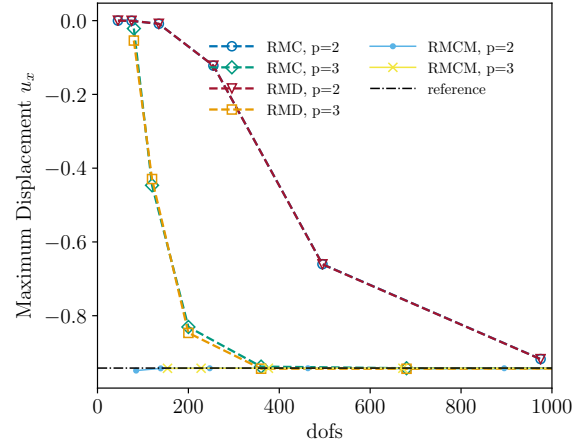
(b) Slenderness $\frac{R}{t} = 1000$.
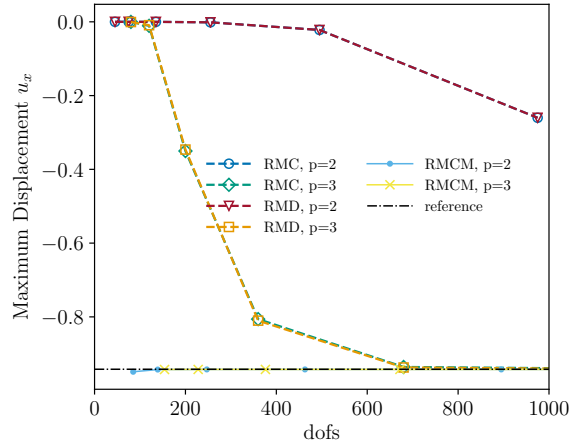
(c) Slenderness $\frac{R}{t} = 10000$.

Figure 5: A cylindrical shell modeled with RMC, RMD and RMCM elements, convergence of maximum tip displacement $u_x$ with increasing slenderness $\frac{R}{t} = 100, 1000, 10000$ and degree $p = 2, 3$.
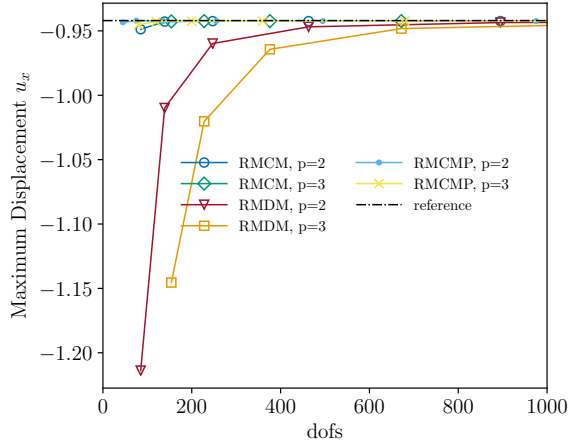
(a) Slenderness $\frac{R}{t} = 100$.
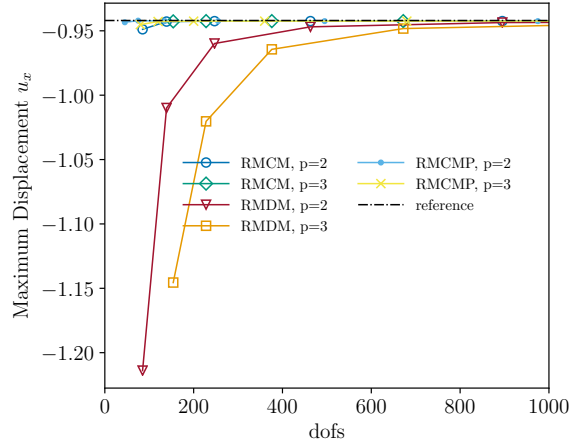
(b) Slenderness $\frac{R}{t} = 1000$.
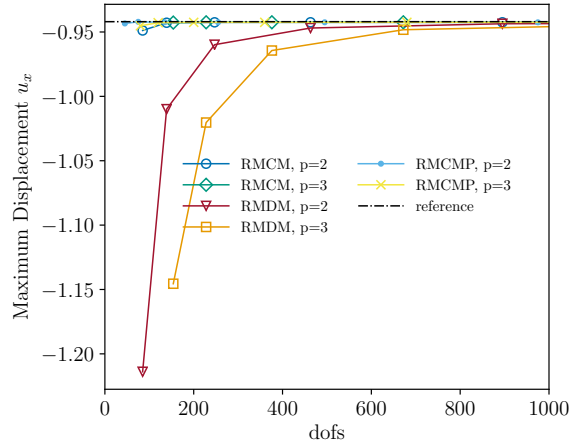
(c) Slenderness $\frac{R}{t} = 10000$.

Figure 6: A cylindrical shell modeled with RMCM, RMDM and RMCMP elements, convergence of maximum tip displacement $u_x$ with increasing slenderness $\frac{R}{t} = 100, 1000, 10000$ and degree $p = 2, 3$.

(a) RMC, $\frac{R}{t} = 100$      (b) RMCM, $\frac{R}{t} = 100$      (c) RMCMP, $\frac{R}{t} = 100$

(d) RMC, $\frac{R}{t} = 1000$      (e) RMCM, $\frac{R}{t} = 1000$      (f) RMCMP, $\frac{R}{t} = 1000$

(g) RMC, $\frac{R}{t} = 10000$      (h) RMCM, $\frac{R}{t} = 10000$      (i) RMCMP, $\frac{R}{t} = 10000$
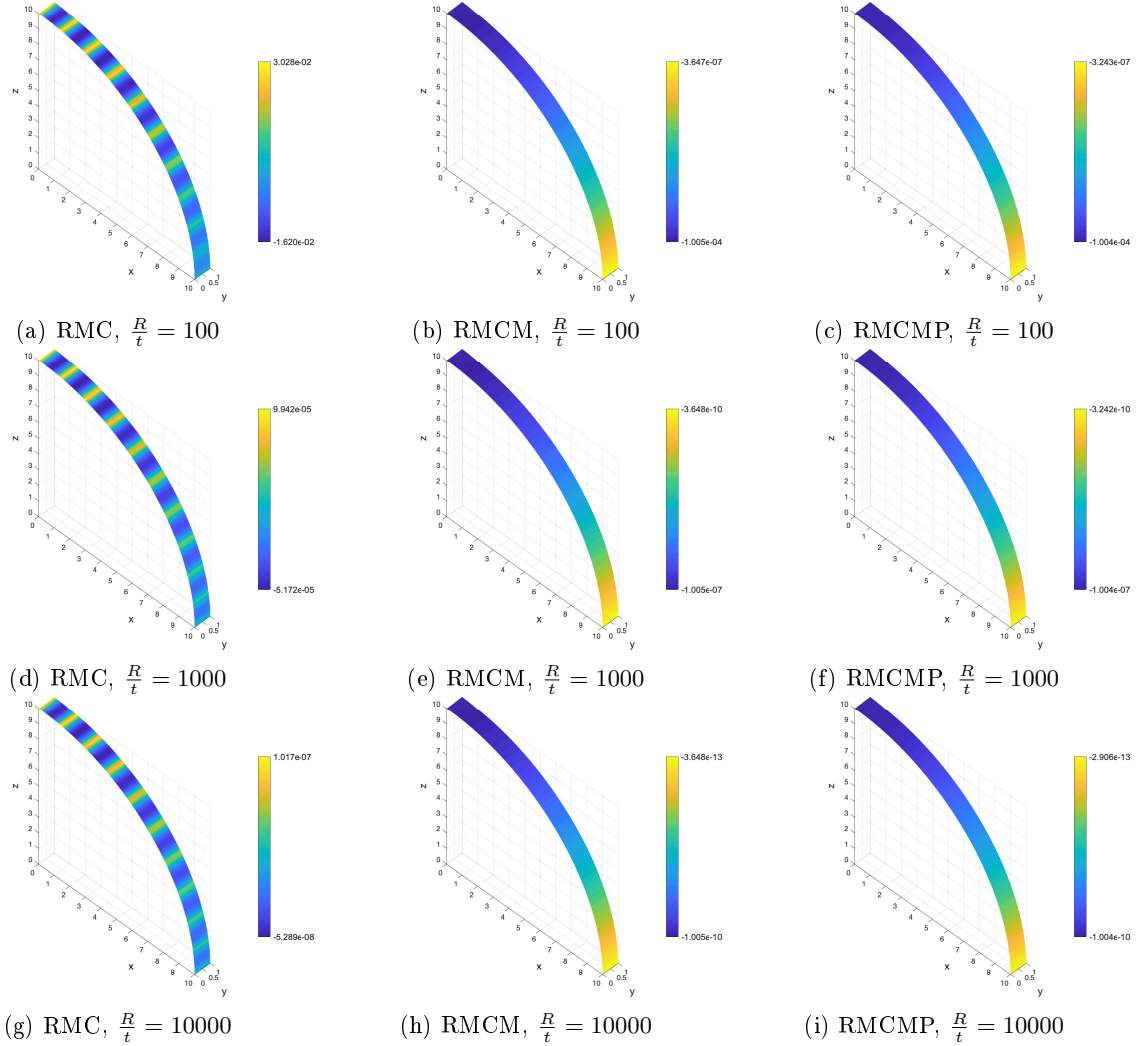
Figure 7: A cylindrical shell, membrane force $n_{\phi\phi}$ for a quadratic $C^1$ cylindrical shell consisting of $10 \times 1$ RMC, RMCM and RMCMP elements, respectively. Exact membrane force: max $= 0$; min $= -0.1t^3$.



(a) Schematic.             (b) Initial quadratic element with skewed control net.
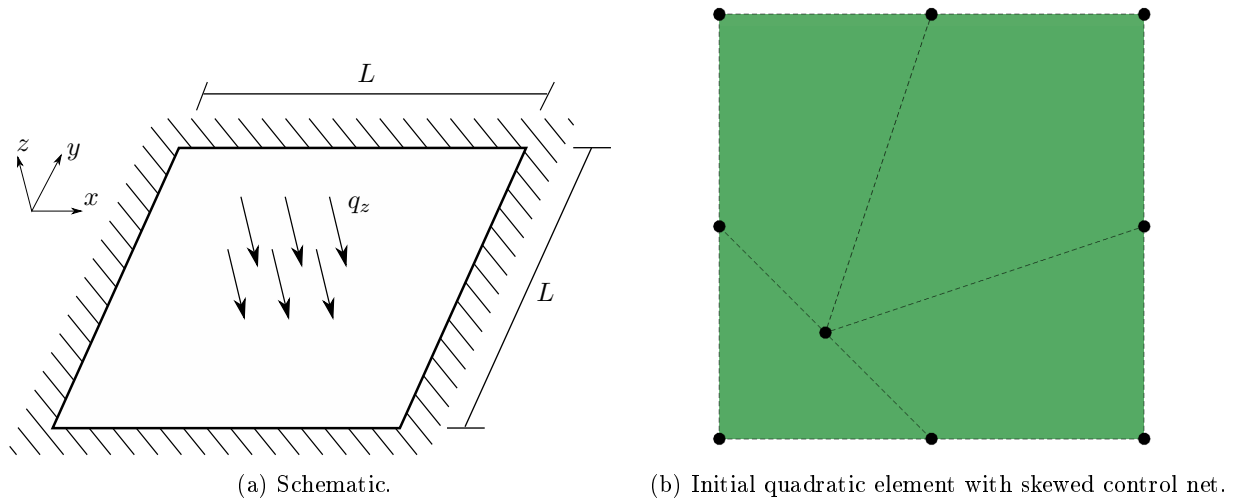
Figure 8: A clamped square plate subject to a uniform distributed load.
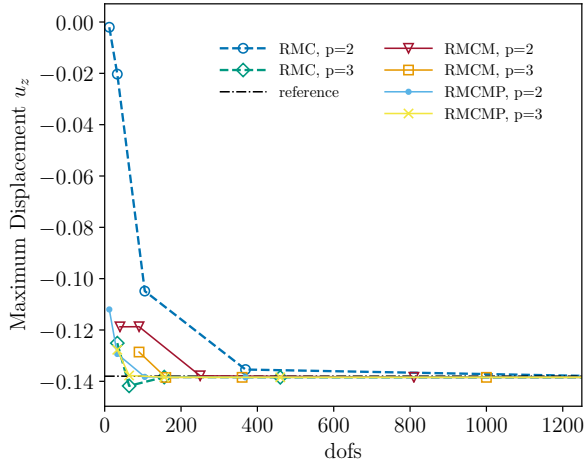
(a) Slenderness $\frac{L}{t} = 100$.
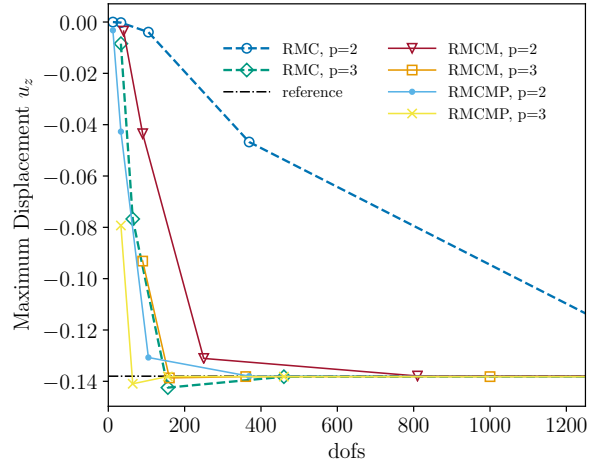
(b) Slenderness $\frac{L}{t} = 1000$.
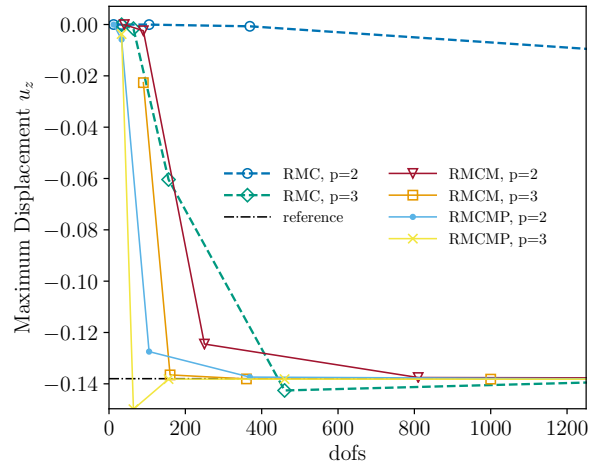
(c) Slenderness $\frac{L}{t} = 10000$.

Figure 9: A clamped square plate under distributed load, maximum deflection $u_z$ for slendernesses $\frac{L}{t} = 100$, 1000, 10000.
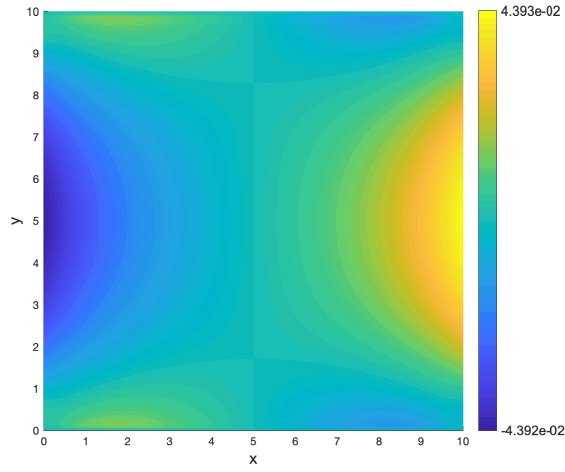
(a) RMC, element $\# = 64 \times 64$, $p = 5$.
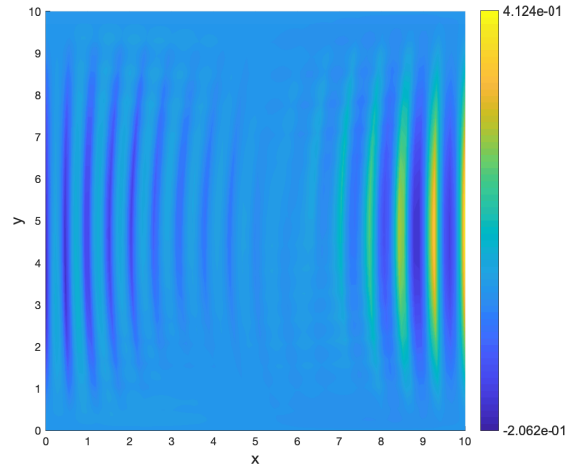
(b) RMC, element $\# = 16 \times 16$, $p = 2$.
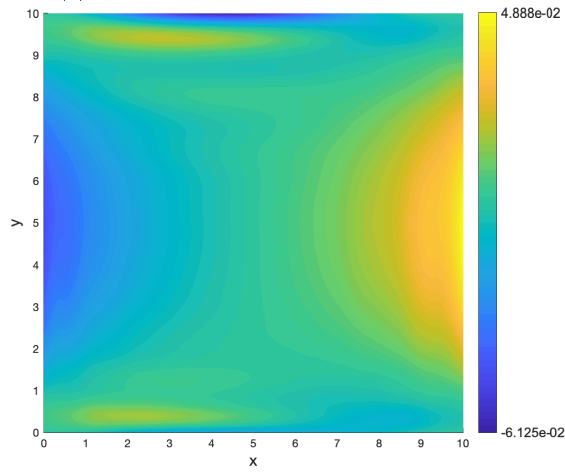
(c) RMCM, element $\# = 16 \times 16$, $p = 2$.
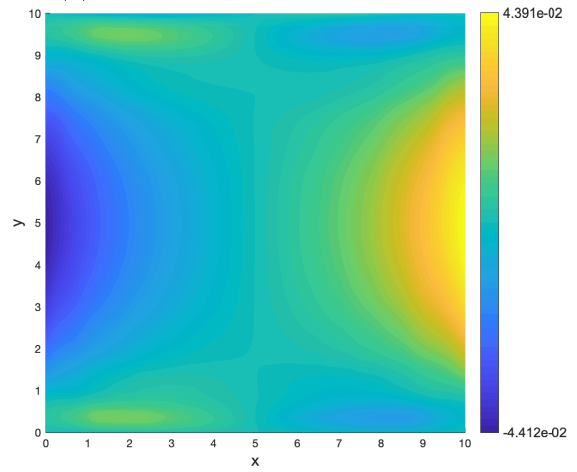
(d) RMCMP, element $\# = 16 \times 16$, $p = 2$.

Figure 10: A clamped square plate under distributed load, shear stress $\sigma_{xz}$ at the midsurface, $\frac{L}{t} = 100$.

## 8.3 Scordelis-Lo roof

The Scordelis-Lo roof problem is part of the shell obstacle course [42] and tests a shell element's ability to handle both membrane and bending modes. An $80°$ arc of a cylinder with radius, $R = 25$, length, $L = 50$, and thickness, $t = 0.25$ or $0.025$ is supported on each end by a rigid diaphragm. It is loaded with its own weight $q_z = 90$. The material has Young's Modulus, $E = 4.32 \times 10^8$, and Poisson's ratio, $\nu = 0$. Figure 11 shows the problem setup.
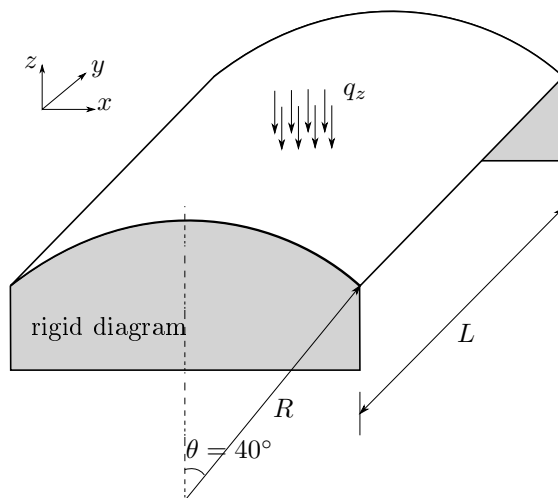


Figure 11: Schematic for the Scordelis-Lo roof problem.



(a) t = 0.25

(b) t = 0.025
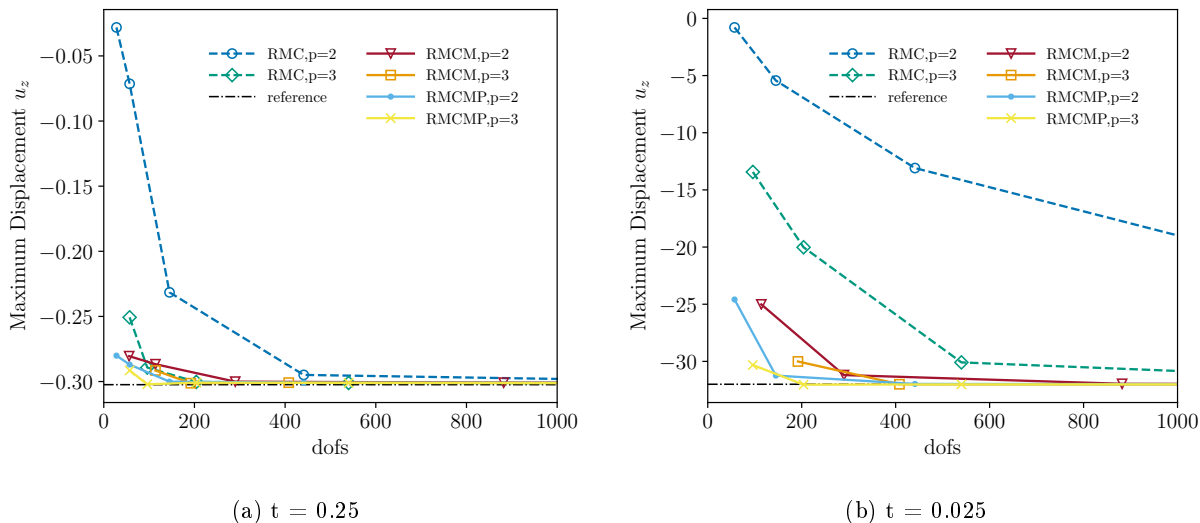
Figure 12: Scordelis-Lo roof, convergence of the maximum displacement, $p = 2, 3$, maximally smooth elements.

The maximum displacement occurs on the free edge at $\frac{L}{2}$. There have been multiple theoretical solutions reported in the literature. The usual FEA solution converges to 0.3024 for $t = 0.25$ [42], and 32 for $t = 0.025$ [25]. Figure 12 shows the convergence behavior of the maximum displacement in terms of degrees of freedom, where only one quarter of the geometry is modeled due to symmetry. The proposed RMCM shell converges faster than the standard RMC shells for all cases in terms of the number of degrees of freedom as shown in Figure 12a and b. Again, RMCMP shell achieves the same results as RMCM shell but with less degrees of freedom as strain variables are condensed out.

23

The proposed shell elements are not only superior in terms of displacement but also in their ability to represent stress fields. A numerical reference for the membrane force $n_{\phi\phi}$ computed using maximally smooth $p = 5$ isogeometric KL shell elements [35] with $50 \times 50$ control points for the whole model is shown in Figure 13a for $t = 0.25$. Figure 13b to d show the membrane force $n_{\phi\phi}$ for $t = 0.25$, $p = 2$. As can be seen, with $17 \times 17$ maximally smooth control points both RMCM and RMCMP obtain accurate and smooth stress resultants while the stresses computed using standard RMC shells oscillate significantly.



(a) KL, pts=$50 \times 50$, $p = 5$.

(b) RMC, pts=$17 \times 17$, $p = 2$.

(c) RMCM, pts=$17 \times 17$, $p = 2$.

(d) RMCMP, pts=$17 \times 17$, $p = 2$.
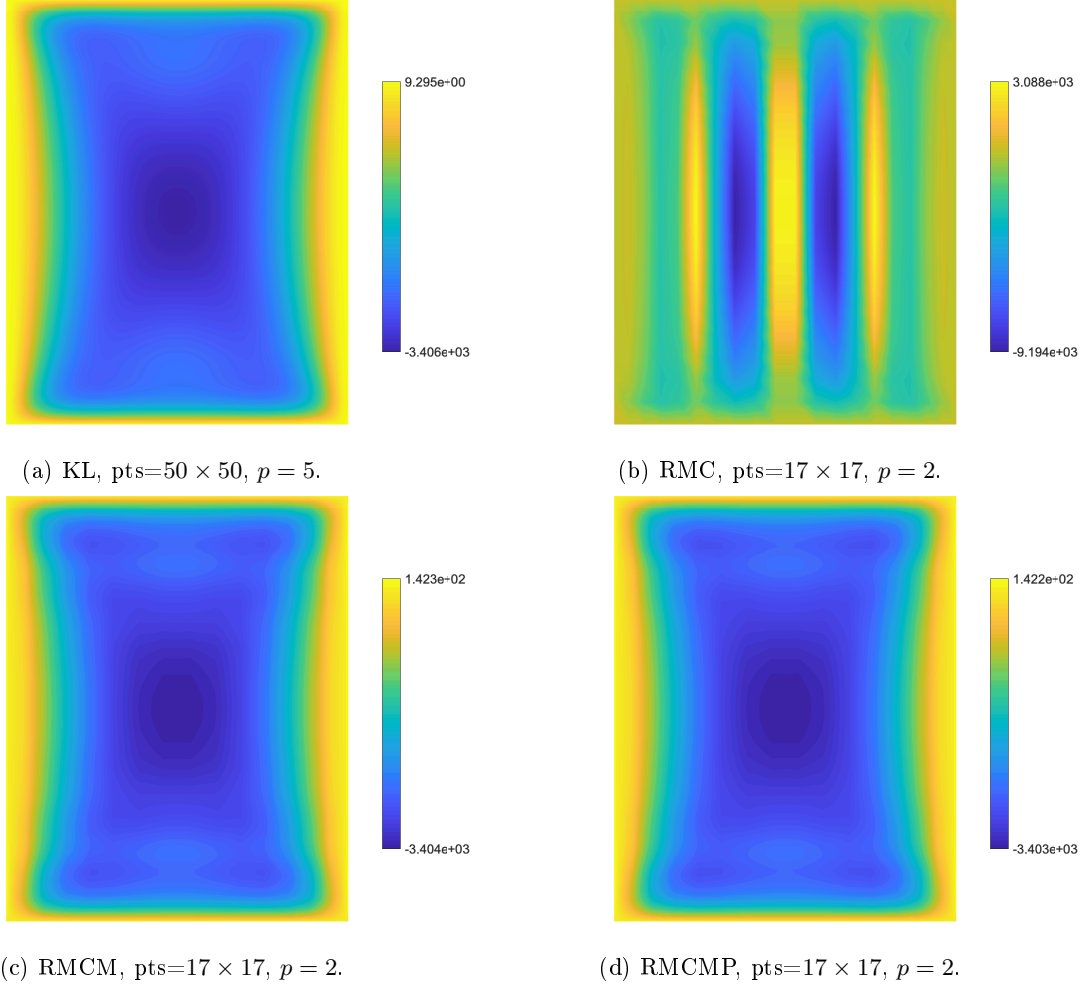
Figure 13: Scordelis-Lo roof, membrane force $n_{\phi\phi}$, $t = 0.25$, maximally smooth elements.

## 8.4 Partly clamped hyperbolic paraboloid

The partly clamped hyperbolic paraboloid problem, proposed in [5], is a widely used test to assess the ability of a shell formulation to address locking in bending-dominated situations [18, 25, 14]. As illustrated in Figure 14, the geometry of the middle surface of the shell is defined by

$$z = x^2 - y^2, \quad (x,y) \in \{(x,y) \mid -L/2 \le x \le L/2, -L/2 \le y \le L/2, L = 1\}.$$

The shell has various thicknesses, $t = 0.01, 0.001$ and $0.0001$, young's modulus, $E = 2 \times 10^{11}$, and Poisson's ratio, $\nu = 0.3$. The structure is clamped along the edge at $x = -L/2$ and is subjected to its self-weight $q_z = 8000t$ per unit area. Due to its symmetry about $xz$-plane, only half of the model is analyzed.

Figure 17 gives the convergence of the vertical displacement, $u_z$, at point $A$. As no analytical solution exists for this problem, slightly different numerical reference solutions are usually used for different shell
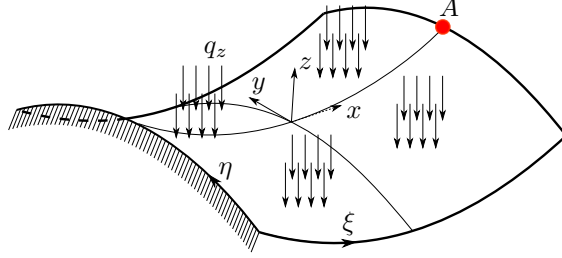
Figure 14: Schematic for the partly clamped hyperbolic paraboloid problem.

Table 1: Clamped hyperbolic paraboloid, reference solutions of displacement and strain energy.

| $t$ | $u_z^{ref}$ | $Ener^{ref}$ |
|------|------------------------------|-----------------------------|
| 0.01 | $-9.3429932 \times 10^{-5}$ | $8.4015268 \times 10^{-3}$ |
| 0.001 | $-6.3973228 \times 10^{-3}$ | $5.5097099 \times 10^{-2}$ |
| 0.0001 | $-5.3045439 \times 10^{-3}$ | $4.4985775 \times 10^{-2}$ |

formulations [5, 25, 14]. In this work, we obtain the numerical reference solutions $u_z^{ref}$ at point $A$, listed in Table 1, with the standard RMC shell and a very fine mesh, i.e., $127 \times 63$ maximally smooth quintic elements. The relative error between the reference solutions given here and those given in [25] are less than 1‰. As can be seen, for both $p = 2$ and 3, the standard RMC shell locks severely as the thickness decreases. The RMCM and RMCMP shells, in contrast, converge much faster than the RMC shell despite it getting slower as the shell gets thinner. The slowdown of convergence for the mixed shells is mainly due to the fact that, as the thickness decreases the energy tends to concentrate to the diagonal lines, it then becomes more challenging to capture the complicated deformation [25].

Figure 16 shows the membrane force $n_{11}$ with different shell formulations, where the subscript 11 of $n_{11}$ denotes that the membrane force is along the base vector $A_1$ direction defined in (15). Figure 16a gives a numerical reference solution with $64 \times 32$ maximally smooth quintic elements. As can be seen, with $2 \times 20$ quadratic elements, the RMCM and RMCMP shells achieve smooth membrane force which are similar to the reference solution while the standard RMC shell shows oscillation. Note that the minimum values obtained by the RMCM and RMCMP shells are different from the reference solution due to the stress concentration happening at the lower left corner.

To better assess the ability of the proposed shell formulations, we also investigate the convergence of the global strain energy in the same manner as studied in [5, 25, 14]. Again, the reference solutions $Ener^{ref}$ are listed in Table 1, which are obtained with the same element type and mesh size as the displacement reference solution $u_z^{ref}$. The convergence curves of the relative energy error for $p = 2$ and various thicknesses are plotted in Figure 17 in log-scale. As can be seen, the convergence rates for RMCM and RMCMP shells do not deteriorate as the shell goes thinner even though the error increases due to the more complicated deformation states as mentioned previously. In contrast, the convergence rate decreases obviously for the standard RMC shell with $t = 0.0001$. It is also noticed that even with comparable convergence rates, the proposed RMCMP shell achieves smaller error than the mixed RMCM shell for $t = 0.001$ and 0.0001, which further demonstrates the effectiveness of the proposed RMCMP shell in alleviating locking.

25
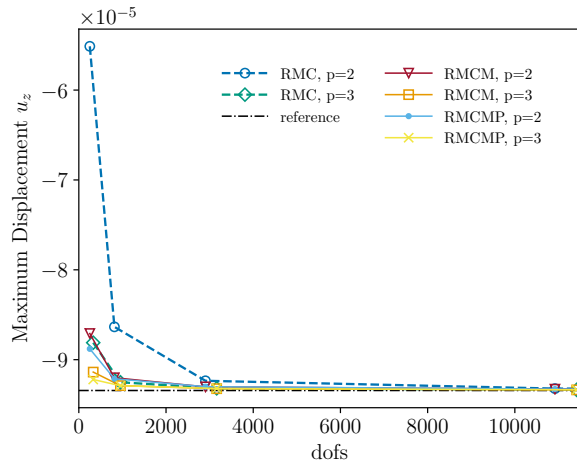
(a) t = 0.01.
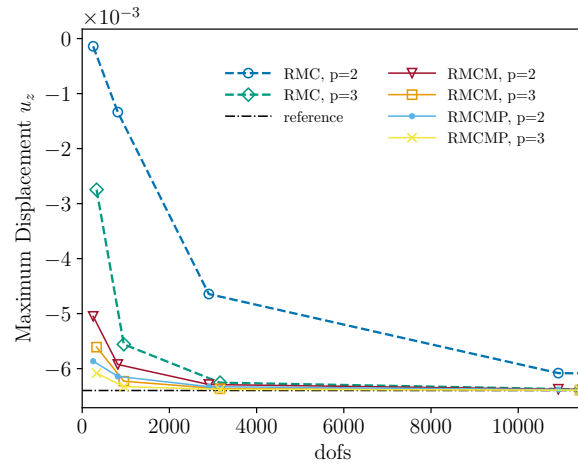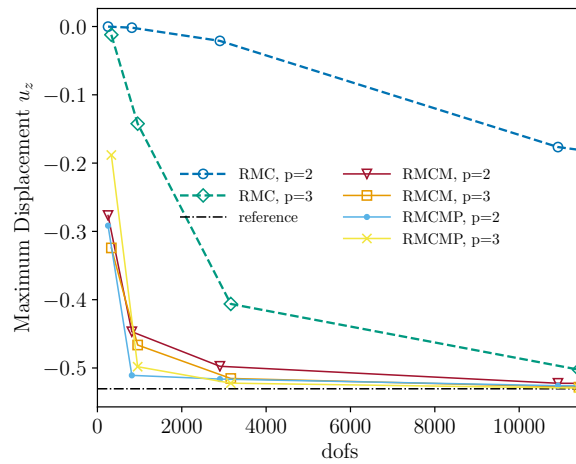
(b) t = 0.001.

(c) t = 0.0001.

Figure 15: Hyperbolic paraboloid, convergence of the displacement $u_z$ at point $A$, $p = 2, 3$, maximally smooth elements.

(a) RMC, element #=$64 \times 32$, $p = 5$.



(b) RMC, element #=$20 \times 20$, $p = 2$.



(c) RMCM, element #=$20 \times 20$, $p = 2$.



(d) RMCMP, element #$20 \times 20$, $p = 2$.
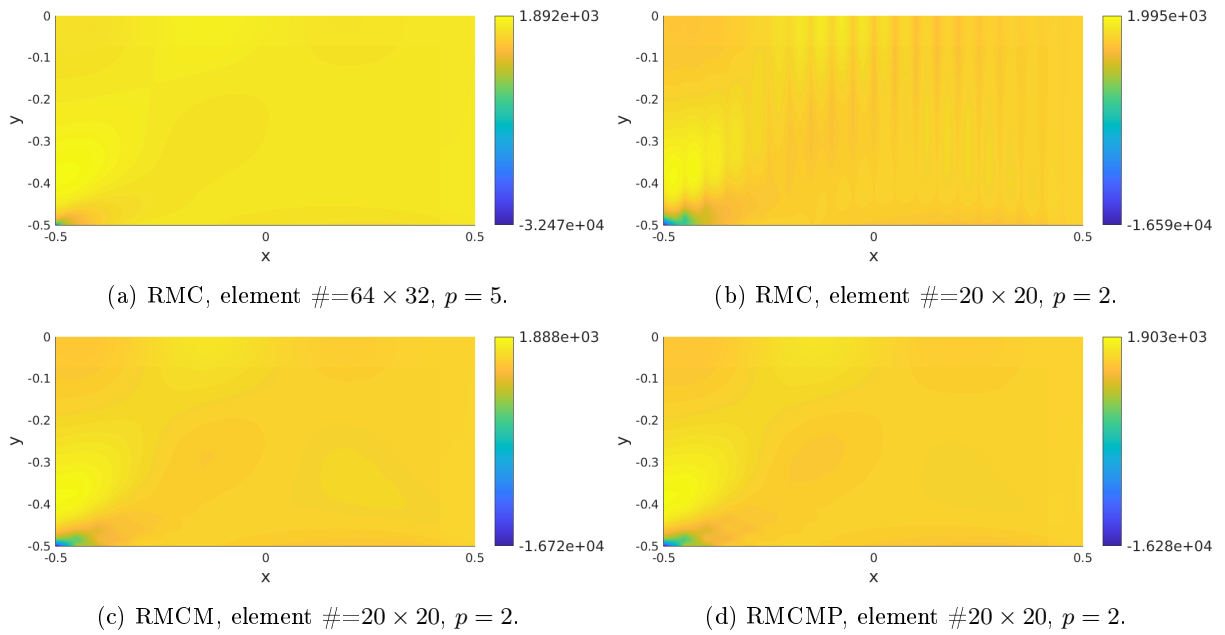
Figure 16: Hyperbolic paraboloid shell, membrane force $n_{11}$, $t = 0.01$, maximally smooth elements.
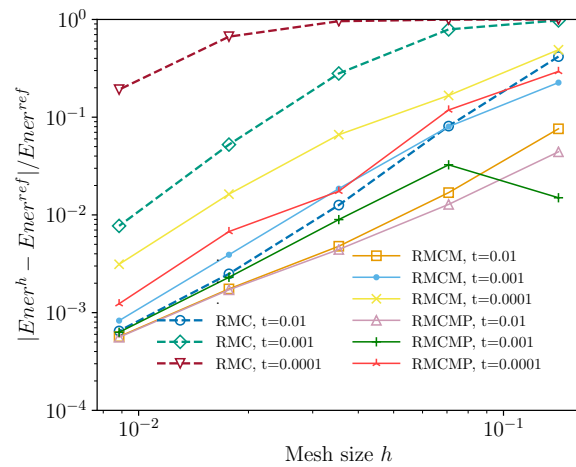


Figure 17: Hyperbolic paraboloid, convergence of the relative strain energy in terms of the mesh size, $p = 2$.

## 8.5 Straight cantilever shell subjected to end moment

In this section, we study the roll-up of the straight cantilever beam (modeled as a shell) shown in Figure 18. This problem is widely used to test the ability of a shell element to handle large rotations. The beam has a length of $L = 12$, width $b = 1$, and thickness $t = 0.1$. It is fixed on one end and subjected to a uniform line moment $m = M/b$ on the free end. The material has Young's modulus, $E = 1.2 \times 10^6$, and Poisson's ratio, $\nu = 0.3$. The analytical solutions of the displacements from the classical flexural theory at the free end are given by $u_x(M) = [\sin(\frac{M}{M_0})\frac{M_0}{M} - 1]L$ and $u_z(M) = [1 - \cos(\frac{M}{M_0})]\frac{M_0}{M}$ with $M_0 = \frac{EI}{L} = \frac{25}{3}$ [51] which hold for the inextensible shells used in this work. The cantilever beam should roll up into an exact circle for $M = 2\pi M_0$ with a free end rotation of $\theta = 2\pi$. These analytical solutions

In this test, the moment $M = 2\pi M_0$ is applied in 10 load steps and the convergence of the free end rotation for maximally smooth B-splines of degree $p = 2$ and 3 are shown in Figure 19. The initial mesh consists of $4 \times 1$ elements. As can be seen, the proposed RMCM shell element obtains $2\pi$ with very coarse meshes for both $p = 2$ and 3. The RMCMP shell obtains the same results as the RMCM shell but with less degrees of freedom. However, the RMDM shell element does not converge for the coarse mesh and even behaves worse than the standard RMC and RMD shells. This can be attributed to the inaccuracies inherent in the discrete rotations for coarse meshes and large rotations. For 10 load steps, the RMC shell requires 64 quadratic elements to converge to a circle, as shown in Figure 20a, while the RMCM and RMCMP shells only need 5 quadratic elements and 7 load steps to achieve a circle, as shown in Figure 20b and c, respectively. The total Newton-Raphson iteration counts and the iteration behavior of the last load step for the different shell formulations are shown in Table 2. The RMCM and RMCMP shells achieve a circle with only 51 and 50 total Newton-Raphson iterations, respectively, compared to 110 iterations for the RMC shell. Note that for RMC shell, the convergence process shows oscillation at iterations 6, 8 and 10 of the last load step, which is due to that the mesh is still not refined enough. If more refined mesh is used, the oscillation disappears. Figure 21 shows the deflection at each load step for the RMCMP shell, which tracks the analytical solution very well. This example demonstrates the superior behavior of the proposed RMCM and RMCMP shells in handling large rotations.

$$L = 12$$
$$b = 1$$
$$t = 0.1$$
$$E = 1.2 \times 10^6$$
$$\nu = 0$$
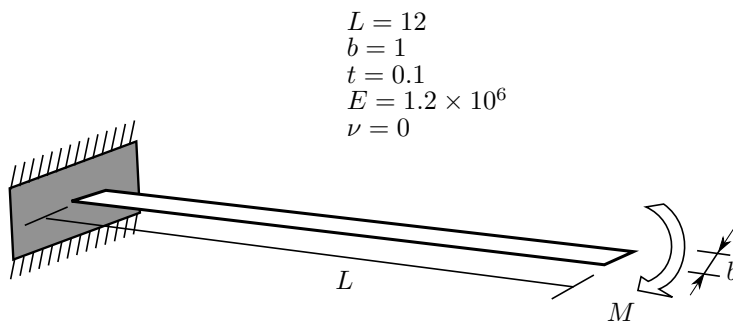


Figure 18: A cantilever shell subjected to an end moment.
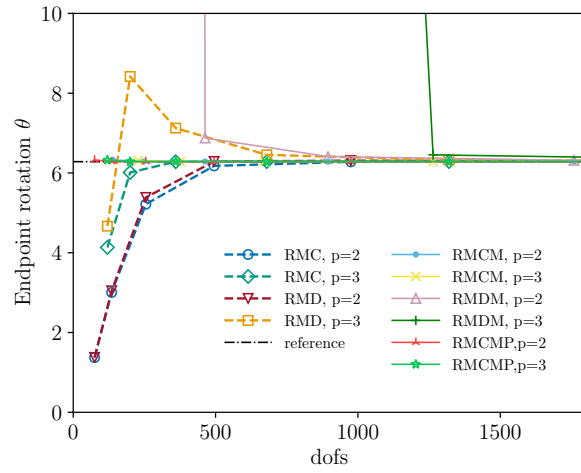
Figure 19: Cantilever beam subjected to an end moment, convergence of the endpoint rotation, $p = 2, 3$, maximally smooth elements, 10 load steps.
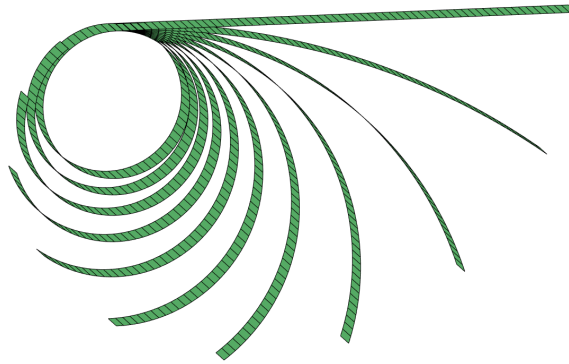


(a) RMC, element $\#= 64 \times 1$, load steps $= 10$.
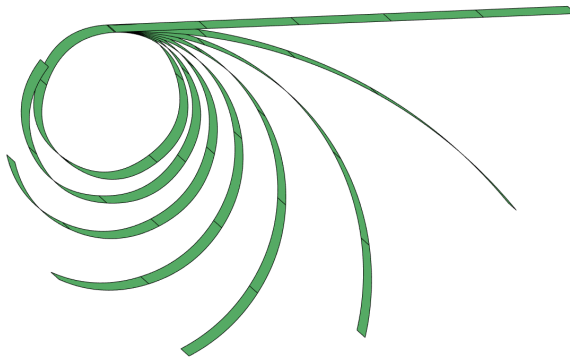


(b) RMCM, element $\# = 5 \times 1$, load steps $= 7$.
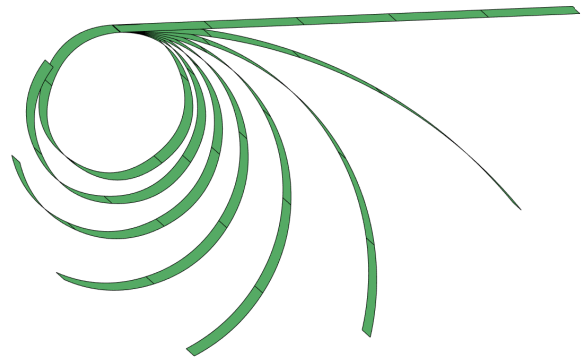


(c) RMCMP, element $\#= 5 \times 1$, load steps $= 7$.

Figure 20: Deformed configurations at each load step for different shell elements, $p = 2$.
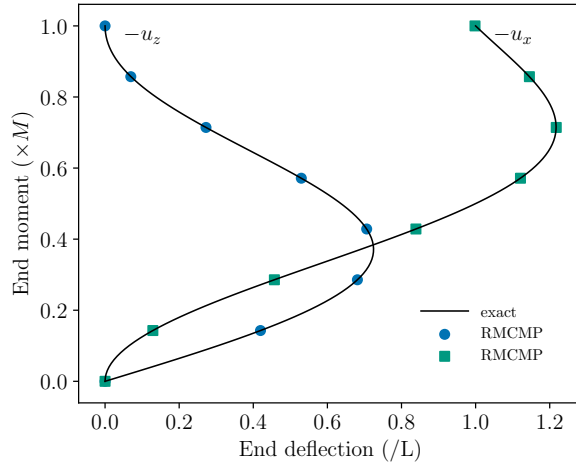
Figure 21: Cantilever beam subjected to an end moment, load-deflection, 5 quadratic maximally smooth elements, 7 load steps.

Table 2: Straight cantilever beam subjected to an end moment: Newton-Raphson iteration behavior of the last load step for RMC, RMCM and RMCMP shells, $p = 2$. A residual norm of $1 \times 10^8$ is used as the tolerance for convergence.

| Last load | Norm of the global residual vector | | |
|---|---|---|---|
| step iterations | **RMC** | **RMCM** | **RMCMP** |
| 1 | 3.0229989 | 4.3185699 | 4.3185699 |
| 2 | 1.7221171e+04 | 1.0305822e+03 | 1.2936436e+02 |
| 3 | 2.6892551e+03 | 4.5473223e+02 | 2.8142369e+01 |
| 4 | 1.2615671e+02 | 2.3987376e+02 | 6.8581274e+01 |
| 5 | 1.7478106 | 1.0344525e+02 | 8.4403519 |
| 6 | 24.185435 | 2.0999644 | 1.0011283e-01 |
| 7 | 0.0609893 | 1.0275647e-02 | 7.1974155e-03 |
| 8 | 2.5605655 | 7.1578287e-07 | 2.9250887e-07 |
| 9 | 9.0084745e-04 | 3.1091745e-11 | 2.1394618e-13 |
| 10 | 0.0023499 | | |
| 11 | 1.2197837e-09 | | |
| Load step # | 10 | 7 | 7 |
| Total iteration # | 110 | 51 | 50 |
| Element # | $64 \times 1$ | $5 \times 1$ | $5 \times 1$ |

## 8.6 Hemispherical shell with hole

The hemispherical shell problem tests a shell element's ability to represent combined membrane and bending modes [41]. The geometry is a hemisphere with radius, $R = 10$, thickness, $t = 0.04$, and an $18°$ hole as shown in Figure 22. The Young's modulus is $E = 6.825 \times 10^7$ and the Poisson's ratio is $\nu = 0.3$. The hemisphere is loaded with four point loads, $P = 200$, on the equator with alternating sign, which results in large deformations and rotations. The reference solution of the radial displacement $u_y$ at point $B$ is -5.86799 [21]. Only one quarter of the hemisphere is modeled due to symmetry.

Figure 23 shows the convergence of the radial displacement at point $B$ for different formulations. The load is applied with 10 equal load steps for $p = 2$ and 3, respectively. In this case, the proposed RMCMP shell converges quickly to the reference solution for both $p = 2$ and 3, which is faster than the RMCM shell. Again, the proposed RMCM shell achieved identical results as the RMCMD shell. To achieve the relative
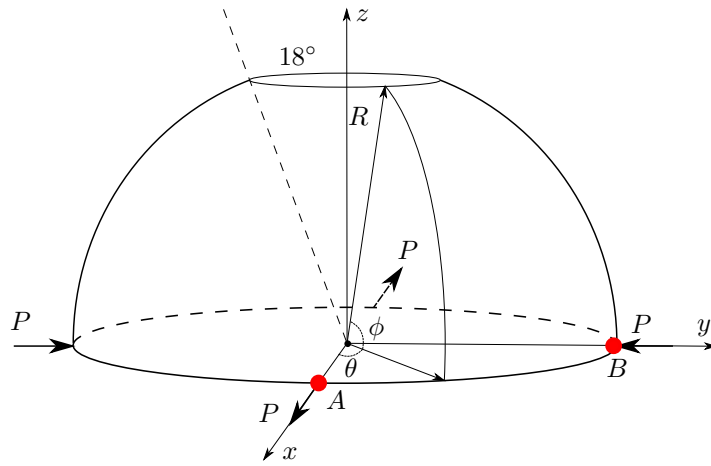
Figure 22: Schematic for the hemispherical shell problem.
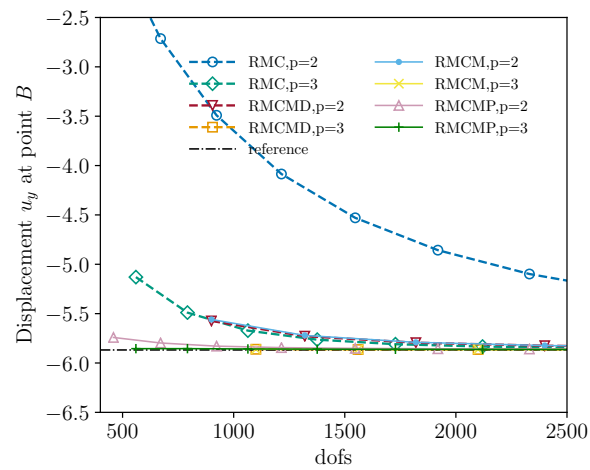


Figure 23: Hemispherical shell with hole. Convergence of the displacement at point $B$, $p = 2, 3$, maximally smooth elements and 10 load steps.
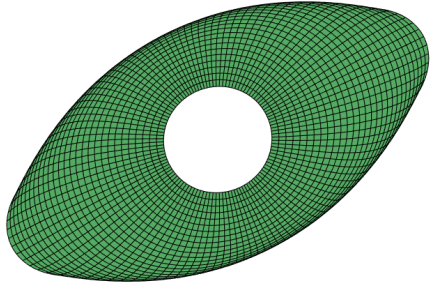
(a) RMC, element $\# = 28 \times 28$.
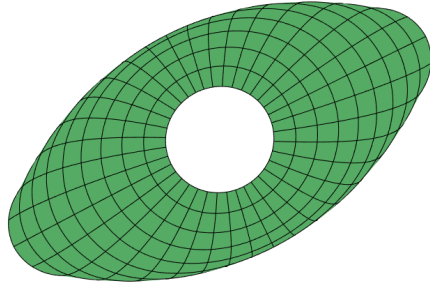


(b) RMCMD, element $\# = 9 \times 9$.
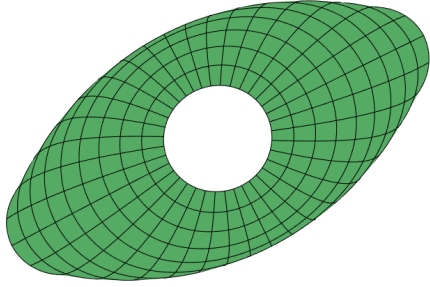


(c) RMCM, element $\# = 9 \times 9$.
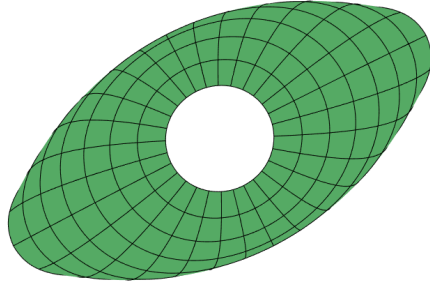


(d) RMCMP, element $\# = 7 \times 7$.

Figure 24: Hemispherical shell with hole. Deformed configurations for RMC, RMCMD, RMCM and RMCMP shells with maximally smooth, quadratic elements and 10 load steps, $|u_B - u_{\mathrm{ref}}|/|u_{\mathrm{ref}}| < 5\%$ at point $B$.

displacement error $|u_B - u_{\mathrm{ref}}|/|u_{\mathrm{ref}}| < 5\%$ at point $B$, the proposed RMCMP shell requires only $7 \times 7$ quadratic elements compared to the standard RMC shell which requires $28 \times 28$ elements. The RMCM and RMCMD shell both need $9 \times 9$ elements. The deformed configurations of the whole hemisphere are created by mirroring the quarter deformed configurations through the symmetric planes, as shown in Figure 24. The Newton-Raphson iteration information for the shell formulations is listed in Table 3. As can be seen, even though RMCM and RMCMP shells require far fewer elements than the RMC shell, they only require 60 total iterations which is less than the 89 iterations required by the RMC shell. RMCMD shell requires more total iterations than the RMCM shell in this case. This is due to the difference between the selectively reduced lower order bases in RMCM and the lower order spaces constructed by taking derivatives of the primal basis in RMCMD. Even though these two bases span the same function space, the individual basis functions differ, which will affect the results slightly.

Table 3: Hemispherical shell with hole: Newton-Raphson iteration behavior for RMC, RMCMD, RMCM and RMCMP shells with 10 load steps, $p = 2$. A residual norm of $1 \times 10^7$ is used as the tolerance for convergence.

| Last load step iterations | Norm of the global residual vector | | | |
|:---:|:---:|:---:|:---:|:---:|
| | **RMC** | **RMCMD** | **RMCM** | **RMCMP** |
| 1 | 1.4142136e+1 | 1.4142136e+1 | 1.4142136e+1 | 1.4142136e+1 |
| 2 | 1.3777805e+4 | 3.4425023e+3 | 4.1793789e+2 | 3.8894389e+1 |
| 3 | 3.4436270e+1 | 2.9080795e+1 | 1.5350666 | 3.4801747e-2 |
| 4 | 1.3510823e+1 | 1.1198335e-2 | 1.7726484e-4 | 2.1305495e-4 |
| 5 | 5.8204885e-1 | 4.1729117e-4 | 7.3943139e-7 | 1.0146852e-6 |
| 6 | 7.0268520e-3 | 1.4014187e-5 | 5.2659190e-9 | 5.6220310e-9 |
| 7 | 2.0814432e-7 | 4.8116486e-7 | | |
| 8 | 2.8150056e-8 | 1.7065087e-8 | | |
| Total iteration # | 89 | 77 | 60 | 60 |
| Element # | $28 \times 28$ | $9 \times 9$ | $9 \times 9$ | $7 \times 7$ |

# 9 Conclusions

We introduce a mixed isogeometric Reissner-Mindlin shell formulation, based on the Hellinger-Reissner variational principle, to overcome both shear and membrane locking and stress oscillations in higher-order continuous elements. In addition to the displacements and rotations, the membrane and shear strains are chosen as unknown fields, which are interpolated with carefully selected lower-order bases.

We propose an efficient technique to condense out the assumed strain variables in the mixed shell formulation. The approach leverages a Bézier dual basis and preserves the sparsity of the global stiffness matrix. Both linear and nonlinear numerical examples show that the condensation approach actually improves the accuracy of the mixed approach on a per degree of freedom basis.

We investigate the accuracy of the mixed shell formulations for both the continuous and discrete rotation concepts. Numerical examples demonstrate that the continuous and discrete rotation concepts achieve similar accuracy for standard RM shells with lower-order bases and small deformations. However, once the shear and membrane locking is removed by the proposed formulation, the discrete rotation concept is less accurate, and even unstable for large deformation problems. This can be attributed to the inaccuracies inherent in projecting the continuous surface normal to the control points, which do not interpolate the surface. We also propose a more computationally efficient scheme to update the current director. Future work includes the study of the stability of the proposed shell formulation and its extension to material nonlinear problems.

# 10 Acknowledgements

# A  Equivalent update schemes of the current director

In [19, 27, 21], the current director and its derivatives are updated as

$$\mathbf{d}^i = \mathbf{R}^i\mathbf{D} \quad \text{and} \quad \mathbf{d}^i_{,\alpha} = \mathbf{R}^i_{,\alpha}\mathbf{D} + \mathbf{R}^i\mathbf{D}_{,\alpha}, \tag{87}$$

where the total rotation tensor $\mathbf{R}^i$ is updated in a multiplicative manner as

$$\mathbf{R}^i = \Delta\mathbf{R}\mathbf{R}^{i-1}, \tag{88}$$

and its derivatives are updated as

$$\mathbf{R}^i_{,\alpha} = \Delta\mathbf{R}_{,\alpha}\mathbf{R}^{i-1} + \Delta\mathbf{R}\mathbf{R}^{i-1}_{,\alpha}. \tag{89}$$

In this way, $\mathbf{R}^i$ and $\mathbf{R}^i_{,\alpha}$ are required to be calculated and stored at each Newton-Raphson iteration.

In fact, if substituting (88) and (89) into (87), we have

$$\mathbf{d}^i = \mathbf{R}^i\mathbf{D} = \Delta\mathbf{R}\mathbf{R}^{i-1}\mathbf{D} = \Delta\mathbf{R}\mathbf{d}^{i-1} \tag{90}$$

and

$$\begin{aligned}
\mathbf{d}^i_{,\alpha} &= \mathbf{R}^i_{,\alpha}\mathbf{D} + \mathbf{R}^i\mathbf{D}_{,\alpha} \\
&= (\Delta\mathbf{R}_{,\alpha}\mathbf{R}^{i-1} + \Delta\mathbf{R}\mathbf{R}^{i-1}_{,\alpha})\mathbf{D} + \Delta\mathbf{R}\mathbf{R}^{i-1}\mathbf{D}_{,\alpha} \\
&= \Delta\mathbf{R}_{,\alpha}\mathbf{R}^{i-1}\mathbf{D} + \Delta\mathbf{R}(\mathbf{R}^{i-1}_{,\alpha}\mathbf{D} + \mathbf{R}^{i-1}\mathbf{D}_{,\alpha}) \\
&= \Delta\mathbf{R}_{,\alpha}\mathbf{d}^{i-1} + \Delta\mathbf{R}\mathbf{d}^{i-1}_{,\alpha}.
\end{aligned} \tag{91}$$

(90) and (91) prove that the proposed director update scheme in (40) and (43) is equivalent to (87). However, it only requires $\mathbf{d}^i$ and $\mathbf{d}^i_{,\alpha}$ are calculated and stored at every Newton-Raphson iteration.

# B  Discretization of the current director based on the continuous rotation concept

In this section and Appendixes C and D, detailed derivations of the discretized director and strain components are given. These derivations are necessary for understanding and implementing the presented geometrically nonlinear RM shell formulations in this work. We note that similar notations and procedures as [27, 19, 21] are used. However, as we define the Green-Lagrange strain components in terms of the contravariant basis vectors in Section 3, the derivatives of different quantities in the following derivations are with respect to the parametric coordinates rather than the local Cartesian coordinates as in [19, 21]. Interested readers are referred to [27, 19, 21] for extra details.

The first variation of $\mathbf{d}$ can be written as

$$\delta\mathbf{d} = \mathbf{W}^{\mathrm{T}}\delta\boldsymbol{\omega}, \quad \mathbf{W} = \text{skew}\,\mathbf{d} \tag{92}$$

and the derivatives can be written as

$$\delta\mathbf{d}_{,\alpha} = \mathbf{W}^{\mathrm{T}}_{,\alpha}\delta\boldsymbol{\omega} + \mathbf{W}^{\mathrm{T}}\delta\boldsymbol{\omega}_{,\alpha}, \quad \mathbf{W}_{,\alpha} = \text{skew}\,\mathbf{d}_{,\alpha}. \tag{93}$$

The second variation of $\mathbf{d}$ can be written as

$$\mathbf{h} \cdot \Delta\delta\mathbf{d} = \delta\boldsymbol{\omega}^{\mathrm{T}}\mathbf{M}(\mathbf{h})\Delta\boldsymbol{\omega}, \tag{94}$$

where

$$\mathbf{M}(\mathbf{h}) = \frac{1}{2}(\mathbf{d} \otimes \mathbf{h} + \mathbf{h} \otimes \mathbf{d}) - (\mathbf{d} \cdot \mathbf{h})\mathbf{I} \tag{95}$$

and $\mathbf{h}$ is an arbitrary vector.

The derivatives of $\Delta\delta\mathbf{d}$ can be written as

$$\mathbf{h} \cdot \Delta\delta\mathbf{d}_{,\alpha} = \delta\boldsymbol{\omega}_{,\alpha}^{\mathrm{T}}\mathbf{M}(\mathbf{h})\Delta\boldsymbol{\omega} + \delta\boldsymbol{\omega}^{\mathrm{T}}\mathbf{M}_{,\alpha}(\mathbf{h})\Delta\boldsymbol{\omega} + \delta\boldsymbol{\omega}^{\mathrm{T}}\mathbf{M}(\mathbf{h})\Delta\boldsymbol{\omega}_{,\alpha}, \tag{96}$$

where

$$\mathbf{M}(\mathbf{h})_{,\alpha} = \frac{1}{2}(\mathbf{d}_{,\alpha} \otimes \mathbf{h} + \mathbf{h} \otimes \mathbf{d}_{,\alpha}) - (\mathbf{d}_{,\alpha} \cdot \mathbf{h})\mathbf{I}. \tag{97}$$

The increment of the axial vector and its derivatives are discretized as

$$\Delta\boldsymbol{\omega}^h = \sum_I^{n_p} N_I \Delta\boldsymbol{\omega}_I = \sum_I^{n_p} N_I \mathbf{T}_{3I} \Delta\boldsymbol{\beta}_I \quad \text{and} \quad \Delta\boldsymbol{\omega}_{,\alpha}^h = \sum_I^{n_p} N_{I,\alpha} \Delta\boldsymbol{\omega}_I = \sum_I^{n_p} N_{I,\alpha} \mathbf{T}_{3I} \Delta\boldsymbol{\beta}_I \tag{98}$$

where

$$\mathbf{T}_{3I} = \begin{cases} [\mathbf{a}_{1I} \quad \mathbf{a}_{2I}] & \text{for nodes in the smooth regions} \\ \mathbf{I}_{3\times 3} & \text{for nodes along kinks} \end{cases} \tag{99}$$

$$\mathbf{a}_{\alpha I} = \Delta\mathbf{R}(\Delta\boldsymbol{\omega}_I)\mathbf{a}_{\alpha I}^{i-1}, \quad \mathbf{a}_{\alpha I}^{i-1} \text{ is the current nodal basis vectors} \tag{100}$$

$$\Delta\boldsymbol{\omega}_I = \mathbf{T}_{3I}\Delta\beta_I. \tag{101}$$

Note that the matrix $\mathbf{T}_{3I}$ in (99) is reduced to the identity along kinks, where the entire rotation vector $\Delta\boldsymbol{\omega}_I$ is used for the $I$th node in the interpolation. In this work, we update the nodal basis vectors in the way as shown in (100) rather than that given in [19, 21] as

$$\mathbf{a}_{\alpha I} = \Delta\mathbf{R}(\Delta\boldsymbol{\omega}_I)\mathbf{R}_I^{i-1}\mathbf{A}_{\alpha I}. \tag{102}$$

In this way, we only need to store the current nodal basis vectors $\mathbf{a}_{\alpha I}^i$ rather than the nodal rotation matrix $\mathbf{R}_I^i$ at each Newton-Raphson and the initial nodal basis vectors $\mathbf{A}_{\alpha I}$. Therefore, the storage and computational cost can be reduced as explained similarly for the update of the current director at quadrature points in Section 4.1.

The first variation of the director and its derivatives are discretized as

$$\delta\mathbf{d}^h = \mathbf{W}^{h\mathrm{T}}\delta\boldsymbol{\omega}^h = \sum_{I=1}^{n_p} \mathbf{T}_I \delta\boldsymbol{\beta}_I \tag{103}$$

$$\delta\mathbf{d}_{,\alpha}^h = \sum_{I=1}^{n_p} \mathbf{T}_{I,\alpha} \delta\boldsymbol{\beta}_I \tag{104}$$

where

$$\mathbf{T}_I = \mathbf{W}^{h\mathrm{T}} N_I \mathbf{T}_{3I} \tag{105}$$

$$\mathbf{T}_{I,\alpha} = [\mathbf{W}_{,\alpha}^{h\mathrm{T}} N_I + \mathbf{W}^{h\mathrm{T}} N_{I,\alpha}]\mathbf{T}_{3I}. \tag{106}$$

The second variation of the director and its derivatives are discretized as

$$\mathbf{h} \cdot \Delta\delta\mathbf{d}^h = \sum_{I=1}^{n_p}\sum_{K=1}^{n_p} \delta\boldsymbol{\beta}_I^{\mathrm{T}}\mathbf{T}_{3I}^{\mathrm{T}} N_I \mathbf{M}^h(\mathbf{h}) N_K \mathbf{T}_{3K}\delta\boldsymbol{\beta}_K = \sum_{I=1}^{n_p}\sum_{K=1}^{n_p} \delta\boldsymbol{\beta}_I^{\mathrm{T}}\hat{\boldsymbol{q}}_{IK}^{\beta\beta}(\mathbf{h})\delta\boldsymbol{\beta}_K \tag{107}$$

$$\mathbf{h} \cdot \Delta\delta\mathbf{d}_{,\alpha}^h = \sum_{I=1}^{n_p}\sum_{K=1}^{n_p} \delta\boldsymbol{\beta}_I^{\mathrm{T}}\mathbf{T}_{3I}^{\mathrm{T}}[N_{I,\alpha}\mathbf{M}^h(\mathbf{h})N_K + N_I \mathbf{M}_{,\alpha}^h(\mathbf{h})N_K + N_I \mathbf{M}^h(\mathbf{h})N_{K,\alpha}]\mathbf{T}_{3K}\delta\boldsymbol{\beta}_K$$

$$= \sum_{I=1}^{n_p}\sum_{K=1}^{n_p} \delta\boldsymbol{\beta}_I^{\mathrm{T}}\hat{\boldsymbol{m}}_{IK,\alpha}^{\beta\beta}(\mathbf{h})\delta\boldsymbol{\beta}_K \tag{108}$$

where

$$\hat{\boldsymbol{q}}_{IK}^{\beta\beta}(\mathbf{h}) = \mathbf{T}_{3I}^{\mathrm{T}} N_I \mathbf{M}^h(\mathbf{h}) N_K \mathbf{T}_{3K} \tag{109}$$

$$\hat{\boldsymbol{m}}_{IK,\alpha}^{\beta\beta}(\mathbf{h}) = \mathbf{T}_{3I}^{\mathrm{T}}[N_{I,\alpha}\mathbf{M}^h(\mathbf{h})N_K + N_I\mathbf{M}_{,\alpha}^h(\mathbf{h})N_K + N_I\mathbf{M}^h(\mathbf{h})N_{K,\alpha}]\mathbf{T}_{3K} \tag{110}$$

and $\mathbf{M}^h(\mathbf{h})$ and $\mathbf{M}_{,\alpha}^h(\mathbf{h})$ are calculated by inserting interpolated values of $\mathbf{h}^h$ and $\mathbf{h}_{,\alpha}^h$ into (95) and (97), respectively.

## C  Discretization of the current director based on the discrete rotation concept

The first variation of the director can be discretized as

$$\delta\mathbf{d}^h = \sum_I N_I \delta\mathbf{d}_I \quad \text{and} \quad \delta\mathbf{d}_{,\alpha}^h = \sum_I N_{I,\alpha} \delta\mathbf{d}_I \tag{111}$$

where

$$\delta\mathbf{d}_I = \mathbf{W}_I^{\mathrm{T}} \delta\boldsymbol{\omega}_I. \tag{112}$$

Following (103) to (104), we have that

$$\delta\mathbf{d}^h = \sum_{I=1}^{n_p} \mathbf{T}_I \delta\boldsymbol{\beta}_I \tag{113}$$

$$\delta\mathbf{d}_{,\alpha}^h = \sum_{I=1}^{n_p} \mathbf{T}_{I,\alpha} \delta\boldsymbol{\beta}_I \tag{114}$$

where

$$\mathbf{T}_I = N_I \mathbf{W}_I^{\mathrm{T}} \mathbf{T}_{3I} \tag{115}$$

$$\mathbf{T}_{I,\alpha} = N_{I,\alpha} \mathbf{W}_I^{\mathrm{T}} \mathbf{T}_{3I}. \tag{116}$$

The second variation of the director can be discretized as

$$\Delta\delta\mathbf{d}^h = \sum_I N_I \Delta\delta\mathbf{d}_I \quad \text{and} \quad \Delta\delta\mathbf{d}_{,\alpha}^h = \sum_I N_{I,\alpha} \Delta\delta\mathbf{d}_I \tag{117}$$

where $\Delta\delta\mathbf{d}_I$ is calculated at each node using (94) as

$$\mathbf{h} \cdot \Delta\delta\mathbf{d}_I = \delta\boldsymbol{w}_I \cdot \mathbf{M}_I(\mathbf{h})\Delta\boldsymbol{w}_I = \delta\boldsymbol{\omega}_I^{\mathrm{T}} \mathbf{M}_I(\mathbf{h})\Delta\boldsymbol{\omega}_I. \tag{118}$$

## D  Discretization of the strain

Substituting $\delta\mathbf{d}^h$ and $\delta\mathbf{d}_{,\alpha}^h$, computed with B or C, into (35) gives the discretized first variation of the strains as

$$\begin{aligned}
\delta\boldsymbol{\epsilon}^h &= \sum_{I=1}^{n_p} \begin{bmatrix} N_{I,1}\bar{\mathbf{x}}_{,1}^{h\mathrm{T}} \\ N_{I,2}\bar{\mathbf{x}}_{,2}^{h\mathrm{T}} \\ N_{I,1}\bar{\mathbf{x}}_{,2}^{h\mathrm{T}} + N_{I,2}\bar{\mathbf{x}}_{,1}^{h\mathrm{T}} \end{bmatrix} \delta\mathbf{u}_I \\
\delta\boldsymbol{\kappa}^h &= \sum_{I=1}^{n_p} \begin{bmatrix} N_{I,1}\mathbf{d}_{,1}^{h\mathrm{T}} & \bar{\mathbf{x}}_{,1}^{h\mathrm{T}}\mathbf{T}_{I,1} \\ N_{I,2}\mathbf{d}_{,2}^{h\mathrm{T}} & \bar{\mathbf{x}}_{,2}^{h\mathrm{T}}\mathbf{T}_{I,2} \\ N_{I,2}\mathbf{d}_{,1}^{h\mathrm{T}} + N_{I,1}\mathbf{d}_{,2}^{hT} & \bar{\mathbf{x}}_{,1}^{h\mathrm{T}}\mathbf{T}_{I,2} + \bar{\mathbf{x}}_{,2}^{h\mathrm{T}}\mathbf{T}_{I,1} \end{bmatrix} \begin{bmatrix} \delta\mathbf{u}_I \\ \delta\boldsymbol{\beta}_I \end{bmatrix} \\
\delta\boldsymbol{\gamma}^h &= \sum_{I=1}^{n_p} \begin{bmatrix} N_{I,1}\mathbf{d}^{h\mathrm{T}} & \bar{\mathbf{x}}_{,1}^{hT}\mathbf{T}_I \\ N_{I,2}\mathbf{d}^{h\mathrm{T}} & \bar{\mathbf{x}}_{,2}^{hT}\mathbf{T}_I \end{bmatrix} \begin{bmatrix} \delta\mathbf{u}_I \\ \delta\boldsymbol{\beta}_I \end{bmatrix}.
\end{aligned} \tag{119}$$

The second variation of the membrane strains (36) are independent of $\mathbf{d}$ so their discretization can be written as

$$\Delta\delta\varepsilon_{\alpha\beta}^h = \frac{1}{2}(\delta\bar{\mathbf{x}}_{,\alpha}^h \cdot \Delta\bar{\mathbf{x}}_{,\beta}^h + \delta\bar{\mathbf{x}}_{,\beta}^h \cdot \Delta\bar{\mathbf{x}}_{,\alpha}^h) = \sum_{I=1}^{n_p}\sum_{K=1}^{n_p} \frac{1}{2}\delta\mathbf{u}_I^T(N_{I,\alpha}N_{K,\beta} + N_{I,\beta}N_{K,\alpha})\mathbf{I}\Delta\mathbf{u}_K. \qquad (120)$$

The bending strains (37) contain both first and second variation information. To simplify the derivation, their discretization can be written in two parts as

$$\Delta\delta\kappa_{\alpha\beta}^h = \frac{1}{2}(\delta\bar{\mathbf{x}}_{,\alpha}^h \cdot \Delta\mathbf{d}_{,\beta}^h + \delta\bar{\mathbf{x}}_{,\beta}^h \cdot \Delta\mathbf{d}_{,\alpha}^h + \delta\mathbf{d}_{,\alpha}^h \cdot \Delta\bar{\mathbf{x}}_{,\beta}^h + \delta\mathbf{d}_{,\beta}^h \cdot \Delta\bar{\mathbf{x}}_{,\alpha}^h + \bar{\mathbf{x}}_{,\alpha}^h \cdot \Delta\delta\mathbf{d}_{,\beta}^h + \bar{\mathbf{x}}_{,\beta}^h \cdot \Delta\delta\mathbf{d}_{,\alpha}^h)$$
$$= \underbrace{\Delta\delta\hat{\kappa}_{\alpha\beta}^h}_{\text{first variation}} + \underbrace{\Delta\delta\hat{\hat{\kappa}}_{\alpha\beta}^h}_{\text{second variation}} \qquad (121)$$

where

$$\Delta\delta\hat{\kappa}_{\alpha\beta}^h = \frac{1}{2}(\delta\bar{\mathbf{x}}_{,\alpha}^h \cdot \Delta\mathbf{d}_{,\beta}^h + \delta\bar{\mathbf{x}}_{,\beta}^h \cdot \Delta\mathbf{d}_{,\alpha}^h + \delta\mathbf{d}_{,\alpha}^h \cdot \Delta\bar{\mathbf{x}}_{,\beta}^h + \delta\mathbf{d}_{,\beta}^h \cdot \Delta\bar{\mathbf{x}}_{,\alpha}^h) \qquad (122)$$

and

$$\Delta\delta\hat{\hat{\kappa}}_{\alpha\beta}^h = \frac{1}{2}(\bar{\mathbf{x}}_{,\alpha}^h \cdot \Delta\delta\mathbf{d}_{,\beta}^h + \bar{\mathbf{x}}_{,\beta}^h \cdot \Delta\delta\mathbf{d}_{,\alpha}^h). \qquad (123)$$

Substituting $\delta\mathbf{d}^h$ and $\delta\mathbf{d}_{,\alpha}^h$ derived in B or C into (122) leads to the discretized variation of the strains

$$\Delta\delta\hat{\kappa}_{\alpha\beta}^h = \frac{1}{2}\sum_{I=1}^{n_p}\sum_{K=1}^{n_p}\{\delta\mathbf{u}_I^T[N_{I,\alpha}\mathbf{T}_{K,\beta} + N_{I,\beta}\mathbf{T}_{K,\alpha}]\Delta\boldsymbol{\beta}_K + \delta\boldsymbol{\beta}_I^T[N_{K,\beta}\mathbf{T}_{I,\alpha}^T + N_{K,\alpha}\mathbf{T}_{I,\beta}^T]\Delta\mathbf{u}_K\}.$$

For the continuous rotation concept substituting (108) into (123) results in

$$\Delta\delta\hat{\hat{\kappa}}_{\alpha\beta} = \frac{1}{2}\sum_{I=1}^{n_p}\sum_{K=1}^{n_p}\delta\boldsymbol{\beta}_I^T(\hat{\boldsymbol{m}}_{IK,\beta}^{\beta\beta} + \hat{\boldsymbol{m}}_{IK,\alpha}^{\beta\beta})\Delta\boldsymbol{\beta}_K.$$

For the discrete rotation concept substituting the second equation of (117) into (123) results in

$$\Delta\delta\hat{\hat{\kappa}}_{\alpha\beta}^h = \frac{1}{2}(\bar{\mathbf{x}}_{,\alpha}^h \cdot \Delta\delta\mathbf{d}_{,\beta}^h + \bar{\mathbf{x}}_{,\beta}^h \cdot \Delta\delta\mathbf{d}_{,\alpha}^h)$$
$$= \frac{1}{2}\sum_{I=1}^{n_p}(\bar{\mathbf{x}}_{,\alpha}^h N_{I,\beta} + \bar{\mathbf{x}}_{,\beta}^h N_{I,\alpha}) \cdot \Delta\delta\mathbf{d}_I$$
$$= \frac{1}{2}\sum_{I=1}^{n_p}\delta\boldsymbol{\omega}_I^T\mathbf{M}_I(\bar{\mathbf{x}}_{,\alpha}^h N_{I,\beta} + \bar{\mathbf{x}}_{,\beta}^h N_{I,\alpha})\Delta\boldsymbol{\omega}_I$$
$$= \frac{1}{2}\sum_{I=1}^{n_p}\delta\beta_I^T\mathbf{T}_{3I}^T\mathbf{M}_I(\bar{\mathbf{x}}_{,\alpha}^h N_{I,\beta} + \bar{\mathbf{x}}_{,\beta}^h N_{I,\alpha})\mathbf{T}_{3I}\Delta\beta_I$$
$$= \frac{1}{2}\sum_{I=1}^{n_p}\sum_{K=1}^{n_p}\delta_{IK}\delta\beta_I^T\mathbf{T}_{3K}^T\mathbf{M}_I(\bar{\mathbf{x}}_{,\alpha}^h N_{I,\beta} + \bar{\mathbf{x}}_{,\beta}^h N_{I,\alpha})\mathbf{T}_{3I}\Delta\beta_K$$
$$= \frac{1}{2}\sum_{I=1}^{n_p}\sum_{K=1}^{n_p}\delta\boldsymbol{\beta}_I^T(\hat{\boldsymbol{m}}_{IK,\beta}^{\beta\beta}(\bar{\mathbf{x}}_{,\alpha}^h) + \hat{\boldsymbol{m}}_{IK,\alpha}^{\beta\beta}(\bar{\mathbf{x}}_{,\beta}^h))\Delta\boldsymbol{\beta}_K$$

where

$$\hat{\boldsymbol{m}}_{IK,\alpha}^{\beta\beta}(\bar{\mathbf{x}}_{,\alpha}^h) = \delta_{IK}N_{I,\alpha}\mathbf{T}_{3I}^T\mathbf{M}_I(\bar{\mathbf{x}}_{,\alpha}^h)\mathbf{T}_{3I}. \qquad (124)$$

37

Similarly, we can get the shear part as

$$\Delta\delta\gamma_\alpha^h = \delta\bar{\mathbf{x}}_{,\alpha}^h \cdot \Delta\mathbf{d}^h + \delta\mathbf{d}^h \cdot \Delta\bar{\mathbf{x}}_{,\alpha}^h + \bar{\mathbf{x}}_{,\alpha}^h \cdot \Delta\delta\mathbf{d}^h$$
$$= \underbrace{\Delta\delta\hat{\gamma}_\alpha}_{\text{first variation}} + \underbrace{\Delta\delta\hat{\hat{\gamma}}_\alpha}_{\text{second variation}} \tag{125}$$

where

$$\Delta\delta\hat{\gamma}_\alpha^h = \sum_I^{n_p} \sum_J^{n_p} \delta\mathbf{u}_I^T N_{I,\alpha} \mathbf{T}_K \Delta\boldsymbol{\beta}_K + \delta\boldsymbol{\beta}_I^T N_{K,\alpha} \mathbf{T}_I^{\mathrm{T}} \Delta\mathbf{u}_K$$

and

$$\Delta\delta\hat{\hat{\gamma}}_\alpha = \sum_I^{n_p} \sum_J^{n_p} \delta\boldsymbol{\beta}_I^T \hat{\boldsymbol{q}}_{IK}^{\beta\beta}(\bar{\mathbf{x}}_{,\alpha}^h)\Delta\boldsymbol{\beta}_K$$

where $\hat{\boldsymbol{q}}_{IK}^{\beta\beta}(\bar{\mathbf{x}}_{,\alpha})$ is defined in (109) for the continuous rotation of the director and

$$\hat{\mathbf{q}}_{IK}^{\beta\beta}(\bar{\mathbf{x}}_{,\alpha}) = \delta_{IK} N_I \mathbf{T}_{3I}^{\mathrm{T}} \mathbf{M}_I(\bar{\mathbf{x}}_{,\alpha}) \mathbf{T}_{3I} \tag{126}$$

for the discrete rotation of the director.

# References

[1] C. Adam, S. Bouabdallah, M. Zarroug, and H. Maitournam. Improved numerical integration for locking treatment in isogeometric structural elements. part II: Plates and shells. *Computer Methods in Applied Mechanics and Engineering*, 284:106–137, February 2015.

[2] U. Andelfinger and E. Ramm. EAS-elements for two-dimensional, three-dimensional, plate and shell structures and their equivalence to HR-elements. *International Journal for Numerical Methods in Engineering*, 36(8):1311–1337, April 1993.

[3] I. Babuška. Error-bounds for finite element method. *Numerische Mathematik*, 16(4):322–333, January 1971.

[4] K.-J. Bathe and E.N. Dvorkin. A formulation of general shell elements—the use of mixed interpolation of tensorial components. *International Journal for Numerical Methods in Engineering*, 22(3):697–722, 1986.

[5] Klaus-Jürgen Bathe, Alexander Iosilevich, and Dominique Chapelle. An evaluation of the MITC shell elements. *Computers & Structures*, 75(1):1–30, March 2000.

[6] L. Beirão Da Veiga, T. J. R. Hughes, J. Kiendl, C. Lovadina, J. Niiranen, A. Reali, and H. Speleers. A locking-free model for Reissner–Mindlin plates: Analysis and isogeometric implementation via NURBS and triangular NURPS. *Mathematical Models and Methods in Applied Sciences*, 25(08):1519–1551, July 2015.

[7] T. Belytschko, J. S.-J. Ong, W. K. Liu, and J. M. Kennedy. Hourglass control in linear and nonlinear problems. *Computer Methods in Applied Mechanics and Engineering*, 43(3):251–276, May 1984.

[8] D. J. Benson, Y. Bazilevs, M.-C. Hsu, and T. J. R. Hughes. Isogeometric shell analysis: The Reissner–Mindlin shell. *Computer Methods in Applied Mechanics and Engineering*, 199(5-8):276–289, January 2010.

[9] D. J. Benson, Y. Bazilevs, M.-C. Hsu, and T. J. R. Hughes. A large deformation, rotation-free, isogeometric shell. *Computer Methods in Applied Mechanics and Engineering*, 200(13-16):1367–1378, March 2011.

[10] D.J. Benson, S. Hartmann, Y. Bazilevs, M.-C. Hsu, and T. J. R. Hughes. Blended isogeometric shells. *Computer Methods in Applied Mechanics and Engineering*, 255:133–146, March 2013.

[11] S. Bieber, B. Oesterle, E. Ramm, and M. Bischoff. A variational method to avoid locking—independent of the discretization scheme. *International Journal for Numerical Methods in Engineering*, 114(8):801–827, May 2018.

[12] M. Bischoff and E. Ramm. Shear deformable shell elements for large strains and rotations. *International Journal for Numerical Methods in Engineering*, 40(23):4427–4449, December 1997.

[13] K.-U. Bletzinger, M. Bischoff, and E. Ramm. A unified approach for shear-locking-free triangular and rectangular shell finite elements. *Computers and Structures*, page 14, 2000.

[14] R. Bouclier, T. Elguedj, and A. Combescure. Efficient isogeometric NURBS-based solid-shell elements: Mixed formulation and $\bar{\mathrm{B}}$ -method. *Computer Methods in Applied Mechanics and Engineering*, 267:86–110, December 2013.

[15] F. Brezzi. On the existence, uniqueness and approximation of saddle-point problems arising from lagrangian multipliers. *Revue française d'automatique, informatique, recherche opérationnelle. Analyse numérique*, 8(R2):129–151, 1974.

[16] N. Büchter, E. Ramm, and D. Roehl. Three-dimensional extension of non-linear shell formulation based on the enhanced assumed strain concept. *International Journal for Numerical Methods in Engineering*, 37(15):2551–2568, August 1994.

[17] J. F. Caseiro, R. A. F. Valente, A. Reali, J. Kiendl, F. Auricchio, and R. J. Alves de Sousa. On the Assumed Natural Strain method to alleviate locking in solid-shell NURBS-based finite elements. *Computational Mechanics*, 53(6):1341–1353, June 2014.

[18] D. Chapelle and K.-J. Bathe. *The Finite Element Analysis of Shells: Fundamentals*. Computational Fluid and Solid Mechanics. Springer, Berlin ; New York, 2nd ed edition, 2011.

[19] W. Dornisch. *Interpolation of rotations and coupling of patches in isogeometric Reissner–Mindlin shell analysis*. PhD thesis, Rheinisch-Westfälische Technische Hochschule Aachen, Fakultät für Bauingenieurwesen, Lehrstuhl für Baustatik und Baudynamik, Aachen, 2015.

[20] W. Dornisch, S. Klinkel, and B. Simeon. Isogeometric Reissner–Mindlin shell analysis with exactly calculated director vectors. *Computer Methods in Applied Mechanics and Engineering*, 253:491–504, January 2013.

[21] W. Dornisch, R. Müller, and S. Klinkel. An efficient and robust rotational formulation for isogeometric Reissner–Mindlin shell elements. *Computer Methods in Applied Mechanics and Engineering*, 303:1–34, May 2016.

[22] R. Echter and M. Bischoff. Numerical efficiency, locking and unlocking of NURBS finite elements. *Computer Methods in Applied Mechanics and Engineering*, 199(5-8):374–382, 2010.

[23] R. Echter, B. Oesterle, and M. Bischoff. A hierarchic family of isogeometric shell finite elements. *Computer Methods in Applied Mechanics and Engineering*, 254:170–180, February 2013.

[24] D. R. Forsey and R. H. Bartels. Hierarchical B-spline refinement. *ACM SIGGRAPH Computer Graphics*, 22(4):205–212, 1988.

[25] L. Greco, M. Cuomo, and L. Contrafatto. A reconstructed local $\bar{\mathrm{B}}$ formulation for isogeometric Kirchhoff–Love shells. *Computer Methods in Applied Mechanics and Engineering*, 332:462–487, April 2018.

[26] L. Greco, M. Cuomo, L. Contrafatto, and S. Gazzo. An efficient blended mixed B-spline formulation for removing membrane locking in plane curved Kirchhoff rods. *Computer Methods in Applied Mechanics and Engineering*, 324:476–511, September 2017.

[27] F. Gruttmann, R. Sauer, and W. Wagner. Theory and numerics of three-dimensional beams with elasto-plastic material behaviour. *International Journal for Numerical Methods in Engineering*, 48(12):1675–1702, 2000.

[28] S. Hosseini, J.J.C. Remmers, C.V. Verhoosel, and R.D. Borst. An isogeometric solid-like shell element for nonlinear analysis. *International Journal for Numerical Methods in Engineering*, 95(3):238–256, July 2013.

[29] H. C. Huang and E. Hinton. A new nine node degenerated shell element with enhanced membrane and shear interpolation. *International Journal for Numerical Methods in Engineering*, 22(1):73–92, January 1986.

[30] T. J. R. Hughes. *The Finite Element Method: Linear Static and Dynamic Finite Element Analysis*. Dover Publications, Mineola, NY, 2000.

[31] T. J. R. Hughes, M. Cohen, and M. Haroun. Reduced and selective integration techniques in the finite element analysis of plates. *Nuclear Engineering and Design*, 46(1):203–222, March 1978.

[32] T. J. R. Hughes, J. A. Cottrell, and Y. Bazilevs. Isogeometric analysis: CAD, finite elements, NURBS, exact geometry and mesh refinement. *Computer Methods in Applied Mechanics and Engineering*, 194(39):4135–4195, October 2005.

[33] T. J. R. Hughes, R. L. Taylor, and W. Kanoknukulchai. A simple and efficient finite element for plate bending. *International Journal for Numerical Methods in Engineering*, 11(10):1529–1543, 1977.

[34] T. J. R. Hughes and T. E. Tezduyar. Finite elements based upon mindlin plate theory with particular reference to the four-node bilinear isoparametric element. *Journal of Applied Mechanics*, 48(3):587, 1981.

[35] J. Kiendl, K.-U. Bletzinger, J. Linhard, and R. Wüchner. Isogeometric shell analysis with Kirchhoff–Love elements. *Computer Methods in Applied Mechanics and Engineering*, 198(49-52):3902–3914, November 2009.

[36] G. Kikis, W. Dornisch, and S. Klinkel. Adjusted approximation spaces for the treatment of transverse shear locking in isogeometric Reissner–Mindlin shell analysis. *Computer Methods in Applied Mechanics and Engineering*, June 2019.

[37] S. Klinkel, F. Gruttmann, and W. Wagner. A mixed shell formulation accounting for thickness strains and finite strain 3d material models. *International Journal for Numerical Methods in Engineering*, 74(6):945–970, May 2008.

[38] F. Koschnick, M Bischoff, N. Camprubí, and K.-U. Bletzinger. The discrete strain gap method and membrane locking. *Computer Methods in Applied Mechanics and Engineering*, 194(21-24):2444–2463, June 2005.

[39] S.W. Lee and J.J. Rhiu. A new efficient approach to the formulation of mixed finite element models for structural analysis. *International Journal for Numerical Methods in Engineering*, 23(9):1629–1641, September 1986.

[40] Q. Long, P. Burkhard Bornemann, and F. Cirak. Shear-flexible subdivision shells: Shear-Flexible Subdivision Shells. *International Journal for Numerical Methods in Engineering*, 90(13):1549–1577, June 2012.

[41] R. MacNeal. *Finite Elements: Their Design and Performance*. M. Dekker, New York, 1994.

[42] R.H. Macneal and R.L. Harder. A proposed standard set of problems to test finite element accuracy. *Finite Elements in Analysis and Design*, 1(1):3–20, April 1985.

[43] D.S. Malkus and T.J.R. Hughes. Mixed finite element methods — Reduced and selective integration techniques: A unification of concepts. *Computer Methods in Applied Mechanics and Engineering*, 15(1):63–81, July 1978.

[44] D. Miao, M.J. Borden, M.A. Scott, and D.C. Thomas. Bézier $\bar{B}$ projection. *Computer Methods in Applied Mechanics and Engineering*, 335:273–297, June 2018.

[45] B. Oesterle, E. Ramm, and M. Bischoff. A shear deformable, rotation-free isogeometric shell formulation. *Computer Methods in Applied Mechanics and Engineering*, 307:235–255, August 2016.

[46] K.C. Park and G.M. Stanley. A curved $C^0$ shell element based on assumed natural-coordinate strains. *Journal of Applied Mechanics*, 53(2):278, 1986.

[47] L.A. Piegl and W. Tiller. *The NURBS Book*. Springer, Berlin ; New York, 2nd edition edition, November 1996.

[48] T.W. Sederberg, D.L. Cardon, G.T. Finnigan, N.S. North, J. Zheng, and T. Lyche. T-spline simplification and local refinement. In *ACM SIGGRAPH 2004 Papers*, SIGGRAPH '04, pages 276–283, New York, NY, USA, 2004. ACM.

[49] T.W. Sederberg, J. Zheng, A. Bakenov, and A. Nasri. T-splines and T-NURCCs. In *ACM SIGGRAPH 2003 Papers*, SIGGRAPH '03, pages 477–484, New York, NY, USA, 2003. ACM.

[50] J.C. Simo and T.J.R. Hughes. On the variational foundations of assumed strain methods. *Journal of Applied Mechanics*, 53(1):51, 1986.

[51] K. Y. Sze, X. H. Liu, and S. H. Lo. Popular benchmark problems for geometric nonlinear analysis of shells. *Finite Elements in Analysis and Design*, 40(11):1551–1569, July 2004.

[52] D.C. Thomas, M.A. Scott, J.A. Evans, K. Tew, and E.J. Evans. Bézier projection: A unified approach for local projection and quadrature-free refinement and coarsening of nurbs and t-splines with particular application to isogeometric design and analysis. *Computer Methods in Applied Mechanics and Engineering*, 284:55–105, 2015.

[53] S. Timoshenko and S. Woinowsky-Krieger. *Theory of Plates and Shells*. McGraw-Hill College, New York, 2 edition edition, June 1959.

[54] W. Wagner and F. Gruttmann. A robust non-linear mixed hybrid quadrilateral shell element. *International Journal for Numerical Methods in Engineering*, 64(5):635–666, October 2005.

[55] J.D. Warren and H. Weimer. *Subdivision Methods for Geometric Design: A Constructive Approach*. Morgan Kaufmann, 2002.

[56] J. Zhang, D. Liu, and Y. Liu. Degenerated shell element with composite implicit time integration scheme for geometric nonlinear analysis: Degenerated Shell Element with Composite Implicit Time Integration. *International Journal for Numerical Methods in Engineering*, 105(7):483–513, February 2016.

[57] O.C. Zienkiewicz, R.L. Taylor, and J.M. Too. Reduced integration technique in general analysis of plates and shells. *International Journal for Numerical Methods in Engineering*, 3(2):275–290, April 1971.

[58] Z. Zou, M. A. Scott, M. J. Borden, D. C. Thomas, W. Dornisch, and E. Brivadis. Isogeometric Bézier dual mortaring: Refineable higher-order spline dual bases and weakly continuous geometry. *Computer Methods in Applied Mechanics and Engineering*, 333:497–534, May 2018.